# Supporting Information

## A Hydroxylated Zwitterion Enables Dual-Modal Synergy for Stable Zinc–Iodine Batteries

Shengchao Chai,[a] Yuxin Zhu,[a] Junpeng Li,[b] Wenxin Xie,[a] Siqi He,[a] Haikun Guo,[a] Yifan Wang,[a] Yizhan Wang,[b] and Haolong Li[a]*

[a] S. Chai, Y. Zhu, W. Xie, S. He, H. Guo, Y. Wang, H. Li
State key laboratory of supramolecular structure and materials, College of Chemistry, Jilin University
Qianjin Avenue 2699, Changchun 130012, China
E-mail: hl_li@jlu.edu.cn

[b] J. Li, Y. Wang
Key Laboratory of Physics and Technology for Advanced Batteries (Ministry of Education), College of Physics, Jilin University
Qianjin Avenue 2699, Changchun 130012, China

## 1. Supplementary Methods[55-73]

### 1.1 Materials

Tripropylamine (99%, Aladdin), Triethanolamine (99%, Aladdin), 1,3-propanesulfonate (99%, Aladdin). $I_2$ (>99.8%, Energy Chemical), $ZnSO_4 \cdot 7H_2O$ (99.995%, Aladdin), The Zn foil (100 μm in thickness), copper foil (20 μm in thickness), polytetrafluoroethylene aqueous dispersion (PTFE, 40 wt.% solid content), Ketjen black (KB), carbon nanotubes (CNTs), titanium mesh, and glass fibers (GF/C, Whatman) were provided by Neware Technology Limited. All of the used solvents were analytical grade.

### 1.2 Instruments

**Matrix-assisted Laser Desorption/Ionization Time-of-Flight (MALDI-TOF) Mass Spectroscopy.** MALDI-TOF spectra were measured on a Bruker Autoflex™ MALDI-TOF mass spectrometer using α-Cyano-4-hydroxycinnamic acid (CHCA) as the matrix. Samples were typically dissolved in $H_2O$ at 1.0 mg $mL^{-1}$. The mass scale was calibrated with polystyrene standards with molecular weight regions under consideration.

**Nuclear Magnetic Resonance (NMR).** $^1H$ NMR spectra (with tetramethylsilane as reference) were recorded on a Bruker AVANCEIII 500 MHz spectrometer at room temperature. Low-field $^1H$ NMR (LF-NMR) was performed using a Niumag MesoMR23-040V low-field spectrometer at 20 MHz proton resonance frequency. Initial parameters were conducted to obtain $T_1$-$T_2$ correlation spectra using an Inversion Recovery-Carr-Purcell-Meiboom-Gill (IR-CPMG) pulse sequence, following initial system calibration via the free induction decay (FID) sequence. The pulse widths were set at 2.32 μs for the 90° pulse and 4.64 μs for the 180° pulse, with the echo time (TE) fixed at 0.3 ms. For the $T_2$ dimension, 5000 echoes were acquired per scan, while the $T_1$ dimension was sampled across 40 logarithmically spaced inversion times. Each of these recovery steps was accumulated over 8 scans. The resulting two-dimensional data set was processed using the simultaneous iterative reconstruction technique (SIRT) algorithm for two-dimensional inverse Laplace transformation, which iteratively reconstructs the $T_1$-$T_2$ correlation map by minimizing the residuals between the experimental data and the bi-exponential kernel model, under the optimized parameters of a 0.1 smoothing factor, 50,000 iterations, and a defined relaxation time range from 0.01 to 100 ms represented by 200 inversion points per dimension.

**X-ray Diffraction (XRD).** XRD patterns were observed on an Empyrean Xray diffractometer (PANalytical B.V.), using Cu Kα1 radiation of a wavelength of 1.542 Å.

**X-ray photoelectron spectroscopy (XPS).** XPS measurements were conducted using a Thermo Fisher ESCALAB $Xi^+$ spectrometer equipped with a monochromatic X-ray source (Al Kα line). Sputtering was performed via a built-in argon ion gun, with the sputter rate calibrated against $SiO_2$ (25 nm $min^{-1}$). Binding energies were calibrated with reference to the C–C signal at 284.8 eV. Sputtering was performed using a monatomic $Ar^+$ ion gun operated at an acceleration voltage of 2 keV and a beam current of 10 μA, with the ion beam rastered over a 1 mm × 1 mm area. The sputter rate was calibrated against a thermally

grown $SiO_2$ reference film under identical conditions, yielding a nominal rate of 1.0 nm $min^{-1}$. These confirm that the depth scale presented in the manuscript is reliable and that the observed gradient in sulfonate concentration is a genuine feature of the interface rather than an artifact of the sputtering process.

**Contact Angle Measurement.** Static contact angle measurements were performed using a Dataphysics OCA20 goniometer. The zinc plate electrodes tested were obtained from zinc symmetric batteries with Bare and $HPS_{50}$ as electrolytes, respectively. These batteries were cycled 5 times under the conditions of 1 mA/$cm^2$ and 1 mAh/$cm^2$. For hydrophobicity comparison, 5 μL water droplets were deposited on the surfaces of these two types of zinc plates. For zinc wettability comparison, 5 μL droplets of 2 M zinc sulfate aqueous solution were used. Static contact angle was adopted as the evaluation index, with at least three measurements taken at different positions on each sample.

**Transmission Electron Microscopy (TEM).** TEM images were performed on a JEM-2100F electron microscope operating at 200 kV. The zinc electrode used was obtained from zinc symmetric batteries with $HPS_{50}$ as the electrolyte, and the battery was cycled 10 times under the conditions of 1 mA/$cm^2$ and 1 mAh/$cm^2$.

**Scanning electron microscope (SEM).** SEM images were performed on a Thermo Quattro S with a primary electron energy of 5 kV. Energy dispersive X-ray spectroscopy (EDS). EDS analysis was performed on Bruker Quantax EDS to investigate the distribution of C, N, S, O elements.

**X-ray Absorption Fine Structure (XAFS) Measurements.** Zn K-edge analysis was performed with Si(111) crystal monochromators at the BL14W1 beamlines at the Shanghai Synchrotron Radiation Facility (SSRF) (Shanghai, China). The XAFS spectra were recorded at room temperature using a 4-channel Silicon Drift Detector (SDD) Bruker 5040. Zn K-edge extended X-ray absorption fine structure (EXAFS) spectra were recorded in transmission mode. The XAFS spectra of the standard sample (Zn foils) was recorded in transmission mode. The spectra were processed and analyzed by the software codes Athena and Artemis.

### 1.3 Electrochemical measurements

Zn||Zn symmetric cells, Zn||Cu half cells, and Zn-$I_2$ full cells were all assembled in the form of CR2032 coin cells, and the glass fiber filters were employed as the separator. All long-cycle tests were conducted using LAND battery testing system (CT3002AU, China). The CA tests, Tafel plots, EIS testing, LSV curves, and CV curves were all acquired by AMETEK VersaSTAT3 station. Chronoamperometry was tested by using Zn||Zn symmetric cells at a fixed overpotential of -150 mV for 600 s. The anti-corrosion performance of the Zn plate in different electrolytes was evaluated via Tafel polarization measurements using a three-electrode configuration, where Ti foil was used as both the working electrode and the counter electrode, and Ag/AgCl served as the reference electrode. LSV was conducted on Zn||stainless-steel half cell at a scanning speed of 1 mV $s^{-1}$ in different electrolytes. Electrochemical impedance spectroscopy (EIS) was measured at a fixed amplitude of 10 mV within a

frequent range from 0.1 Hz to 100KHz.

AC Electrochemical Impedance Measurements. The conductivity was measured with a Solartron 1260A impedance/gain-phase analyzer by a two-probe AC impedance method from 0.1 Hz to 100 kHz with the amplitude voltage of the signal at 20 mV. Experiments were performed in a heating/drying oven with program control and forced convection. Each test temperature was stabilized for 15 minutes. The samples were placed in the groove of Teflon mold and sandwiched between two flat copper electrodes. The proton conductivity (σ) was calculated by Equation S1:

$$\sigma = {}^{L}/_{RS} \tag{1}$$

where L (cm) is the distance between two electrodes (The length of the mold groove is 1 cm.), R (Ω) is the high-frequency intercept (charge-transfer resistance) in the Nyquist plot and S ($cm^2$) is the cross-sectional area of the electrodes. The relationship between conductivity and activation energy is consistent with the Arrhenius equation. From the slope, the activation energy ($E_a$) of conductivity can be evaluated using Equation S2:

$$\sigma T = \sigma_0 \exp(-E_a / \kappa T) \tag{2}$$

where $E_a$ denotes the activation energy of conductivity, $\sigma_0$ is the pre-exponential factor, $T$ is the temperature and $\kappa$ is the Boltzmann constant.

Cathode electrodes were prepared by mixing KB with CNTs and PTFE in an 8:1:1 mass ratio and pressing them onto Ti mesh. Then, dissolve 3 g of iodine powder in 10 ml of absolute ethanol. Add the ethanol solution of iodine dropwise to the surface of the aforementioned carbon-based cathode in successive portions, allow it to stand for 6 hours, then dry it and leave it to stand for another 24 hours.

For button cells, the $I^-/I_2$ redox couple was investigated using the cyclic voltammetry technique in the voltage range 0.3-1.8 V. Galvanostatic discharge/charge measurements were conducted at a potential range of 0.3-1.8 V. All current densities were calculated based on the mass of iodine in cathode. Both the tests for the evolution of charge transfer resistance with potential and the oxidation/reduction peak potential differences versus scan rates were conducted using button cells with an iodine loading of 4.5 mg $cm^{-2}$.

The cathode fabrication for the pouch cell follows essentially the same protocol used for the coin-type cells. Ketjen black (KB) and carbon nanotubes (CNTs) serve as the iodine host framework, and polytetrafluoroethylene (PTFE) is employed as the binder. A uniform carbon slurry was first prepared by mixing KB, CNTs, and PTFE in a mass ratio of 8:1:1, and this slurry was manually blade-coated onto a titanium mesh current collector to form the cathode substrate. After drying, the coated electrode sheet was cut into rectangular pieces measuring 60 mm × 60 mm. Iodine was introduced into the carbon host by drop-casting a concentrated solution of iodine dissolved in anhydrous ethanol onto the cathode surface in several successive additions. The cathode was then left to stand under ambient conditions for 12 hours to allow slow evaporation of the ethanol, followed by a gentle heating step to

ensure complete removal of residual solvent.

For pouch cell assembly, a zinc foil anode with dimensions of 65 mm × 65 mm was paired with the iodine cathode. A glass fiber separator (GF/C) was thoroughly soaked with the electrolyte (2 M $ZnSO_4$ with 50 mM HPS) before being sandwiched between the two electrodes. The electrode stack was then inserted into an aluminum–plastic pouch bag, and the cell was sealed using a heat sealer at approximately 120 °C for 5 seconds, leaving a small opening for electrolyte replenishment if necessary. The electrochemical performance of Zn–$I_2$ pouch cells was conducted at a potential range of 0.3-1.8 V under the ambient environment.

UV-vis spectra were collected on an ultraviolet-visible spectrophotometer (Varian Cary 50). *In-situ* UV-vis spectra were acquired by attached cathode and Zn anode on the two sides of quartz cell, and the electrolyte was fulfilled into the quartz cell. Galvanostatic chargedischarge curves of Zn–$I_2$ batteries were collected on the AMETEK VersaSTAT3 station, and UV-vis spectra were used to in-situ monitor the polyiodide dissolution. *In situ* UV-vis validation of $I_3^-$ capture capability at HPS-modified interfaces, where the concentration of $I_3^-$ in the replaced electrolyte was set to 10 mM $L^{-1}$ for this test.

The $Zn^{2+}$ transference number was measured using the Bruce–Vincent method, combining galvanostatic polarization with electrochemical impedance spectroscopy. Measurements were performed in Zn||Zn symmetric coin cells with a defined geometry: Zn foil electrodes 10 mm in diameter and (active area 0.785 $cm^2$), a glass fiber separator (Whatman GF/C) of 12 mm diameter, and an electrolyte volume of 90 μL. The $Zn^{2+}$ transference number ($t$) was determined via the equation:

$$t=I_0(\Delta V-I_sR_s) / I_s(\Delta V-I_0R_0)$$

where $I_0$ and $I_s$ are the initial and steady-state currents (μA) from the chronoamperometry curve, $R_0$ and $R_s$ are the impedance (Ω) before and after the test, and $\Delta V$=10 mV.

### 1.4 Synthesis

#### 1.4.1 Synthesis of 3-(tris(2-hydroxyethyl)ammonio)propane-1-sulfonate (Abbreviated as HPS).

Triethanolamine (14.9 g) and 1,3-propanesulfonate (12.2 g) were added to 50 mL of ethyl acetate. The mixture solution was heated at 40 °C and stirred for 3 days. A white precipitate was formed, which was filtered, washed with ethyl acetate three times, and dried in vacuum. $^1$H NMR (500M, $D_2O$): δ (ppm) = 3.99 (p, 6H, −C**H**$_2$OH), 3.63 (t, 6H, −C**H**$_2$CH$_2$OH), 3.60 (m, 2H, −C**H**$_2$CH$_2$CH$_2$S−), 2.90 (t, 2H, −CH$_2$CH$_2$C**H**$_2$S−), 2.18 (p, 2H, −CH$_2$C**H**$_2$CH$_2$S−) (**Figure S1**). The MALDI-TOF spectrum of HPS exhibited a peak at 272.2, well consistent with HPS+$H^+$ ($C_9H_{21}NO_6SH^+$) whose molecular weight of PPS is 271.1, thus confirming the expected composition of HPS (**Figure S2**).

#### 1.4.2 Synthesis of 3-(tripropylammonio)propane-1-sulfonate (Abbreviated as PPS).

Tripropylamine (24.9 g) and 1,3-propanesulfonate (19.9 g) were added to 100 mL of acetonitrile. The mixture solution was cooled to 0 °C by an ice base and stirred at this temperature for 60 min. Then the ice base was removed and stirred for 1 day. A white precipitate was formed, which was filtered, washed with acetonitrile three times, and dried in vacuum. $^1$H NMR (500M, $D_2O$): δ (ppm) = 3.33 (p, 2H,

−C**H**$_2$CH$_2$CH$_2$S−), 3.14 (p, 6H, −NC**H**$_2$CH$_2$CH$_3$), 2.90 (t, 2H, −C**H**$_2$S−), 2.08 (m, 2H, −CH$_2$C**H**$_2$CH$_2$S−), 1.66 (m, 6H, −NCH$_2$C**H**$_2$CH$_3$), 0.89 (t, 9H, −NCH$_2$CH$_2$C**H**$_3$) (**Figure S19**). The MALDI-TOF spectrum of PPS exhibited a peak at 266.0, well consistent with PPS+H$^+$ ($C_{12}H_{27}NO_3SH^+$) whose molecular weight of PPS is 265.2, thus confirming the expected composition of PPS (**Figure S20**).

### 1.4.3 Preparation of electrolytes

$ZnSO_4 \cdot 7H_2O$ was employed as the solute, with purified water serving as the solvent, to prepare a 2 mol L$^{-1}$ zinc sulfate electrolyte in a 100 mL volumetric flask. For the three additive systems ($HPS_1$, $HPS_{50}$, and $PPS_{50}$), the respective additives at their pre-determined concentrations were co-introduced into 100 mL volumetric flasks along with zinc sulfate heptahydrate. Subsequent to solvent addition and volume adjustment to the calibration mark, 2 mol L$^{-1}$ zinc sulfate electrolytes containing different additives were successfully fabricated.

## 1.5 Computational methods

*Density functional theory*: All density functional theory (DFT) computations were carried out using the Vienna Ab initio Simulation Package (VASP).[55, 56] The Perdew–Burke–Ernzerhof (PBE) functional within the generalized gradient approximation (GGA) was employed to treat the exchange–correlation interactions.[57] The projector augmented wave (PAW) method was used to describe electron–ion interactions.[58] A plane-wave energy cutoff of 400 eV was applied, and a 3 × 3 × 1 Monkhorst–Pack k-point mesh was adopted for sampling the Brillouin zone. Geometric and electronic convergence criteria were set to $10^{-4}$ eV for energy and 0.02 eV Å$^{-1}$ for forces, respectively. Dispersion corrections were incorporated using the DFT-D3 method to account for van der Waals (vdW) interactions.[59] Structural models and electron density data were visualized using VESTA software.[60] The adsorption energy ($E_{ads}$) of an adsorbate A on a substrate was calculated as:

$$E_{ads} = E_{*A} - E_A - E_{sub}$$

where $E_{*A}$ is the total energy of the substrate with adsorbed species A, $E_A$ is the energy of the free molecule A in the gas phase, and $E_{sub}$ is the energy of the clean substrate.

*Molecular dynamics* (Reconstructing solvation structure via zwitterion): Classic molecular dynamics (MD) simulations were performed to explore the mixed solution at the atomic scale. Two bulk systems (System 1 and System 2) were constructed for MD simulations. Initial configurations of the systems were generated using the PACKMOL software,[61] with all molecules randomly placed within a cubic simulation box.

The OPLS-AA force field [62] was utilized to parameterize Zn, $SO_4^{2-}$, HPS, and $H_2O$ species. CM5 charges were assigned, and a 0.7-fold charge scaling was applied to characterize $ZnSO_4$. This approach has been validated by numerous studies[63] and is capable of eliminating average charge screening induced by polarization and charge transfer. The molecular force field comprises nonbonded and bonded interactions. Nonbonded interactions include van der Waals (vdW) and electrostatic components,

described by Equations 1 and 2, respectively:

$$E_{LJ}(r_{ij}) = 4\varepsilon_{ij}\left(\left(\frac{\sigma_{ij}}{r_{ij}}\right)^{12} - \left(\frac{\sigma_{ij}}{r_{ij}}\right)^{6}\right) \quad (3)$$

$$E_c\left(r_{ij}\right) = \frac{q_i q_j}{4\pi\varepsilon_o\varepsilon_r r_{ij}} \quad (4)$$

In the equation, $q_i$、$q_j$ are atomic charge, $r_{ij}$ is the distance between atoms, $\sigma$ is the atomic diameter, $\varepsilon$ is the atomic energy parameter.

For distinct atomic species, geometric mixing rules were employed for vdW interactions, as given by Equation 3:

$$\sigma_{ij} = \left(\sigma_{ii} * \sigma_{jj}\right)^{\frac{1}{2}}; \varepsilon_{ij} = \left(\varepsilon_{ii} * \varepsilon_{jj}\right)^{\frac{1}{2}} \quad (5)$$

The cutoff distance for vdW and electrostatic interactions was set to 1.2 nm, with the particle-mesh Ewald (PME) method used to compute long-range electrostatic interactions.

For the simulations, energy minimization was first performed to relax the simulation box. Subsequently, an isothermal-isobaric (NPT) ensemble with a 1.0 fs time step was used to optimize the simulation box, with temperature and pressure set to 298.15 K and 1.0 atm, respectively. Temperature and pressure were maintained using a Nose-Hoover thermostat and Parrinello-Rahman barostat, respectively. The NPT optimization duration was set to 12.0 ns, sufficient to achieve a stable box size. Thereafter, another NPT simulation with a 1.0 fs time step was run for 1.0 ns to record atomic trajectories (sampled every 1000 fs) for subsequent analysis, with temperature maintained at 298.15 K.

In all MD simulations, atomic motion was described by classical Newtonian equations, solved using the velocity-Verlet algorithm. All MD simulations were executed using the GROMACS 2022.2 package.[64] Results were analyzed using GROMACS toolkits, the Visual Molecular Dynamics (VMD) program.[65]

*Molecular dynamics* ($I_3^-$ adsorption at the HPS-modified cathode interface): Classic molecular dynamics simulations were carried out to investigate the confined system at the atomic level. One confined system was constructed for this purpose. The initial configuration was built using PACKMOL,[61] with $Zn^{2+}$, $SO_4^{2-}$, $H_2O$, $I_3^-$, and HPS molecules randomly inserted into a cubic simulation box above a graphite substrate. The initial configuration of System is illustrated below.

The OPLS-AA force field[66] was used to describe all species, including the graphite substrate. CM5 charges were applied to the molecules, and a 0.7-fold charge scaling was used for $Zn^{2+}$ and $SO_4^{2-}$ ions, consistent with the methodology applied in the bulk systems. Non-bonded interactions (van der Waals and electrostatic) were treated as given in Equations (3) and (4) in the previous section, with geometric mixing rules applied for cross interactions (Equation (5)). A cutoff of 1.2 nm was used for both vdW and electrostatic interactions. Long-range electrostatics were handled with the PME method.

Simulations were performed in the canonical (NVT) ensemble. After energy minimization, an external acceleration corresponding to 1 atm was applied to $Zn^{2+}$, $SO_4^{2-}$, $H_2O$, $I_3^-$ ions along the confined direction. The system was equilibrated for 20 ns with a time step of 2 fs at 298.15 K, maintained using the Nosé–Hoover thermostat.

All integrations were performed using the velocity-Verlet algorithm within GROMACS 2022.2. [64] Trajectory analysis and visualization were conducted using OVITO,[67] in addition to standard GROMACS tools and custom scripts.

*Electrostatic potential*: The electronic structures for SiW, HPS, and PPS were studied via density functional theory, where all geometries were optimized by PBE0[68] functional and def2-TZVP[69, 70] basis set by Gaussian 16. C02 quantum chemical package[71]. The van der Waals interactions were considered by the D3 version of Grimme's dispersion with Becke-Johnson damping[72]. The harmonic frequencies were performed at the same level to confirm that all studied structures as minima possesses zero frequency, i.e. they are located at the minima at the potential energy surfaces. The electrostatic potential for studied molecules was calculated by Multiwfn 3.8 (dev)[73] and plotted by VESTA 3.5.5[60].

## 2. Supplementary Figures

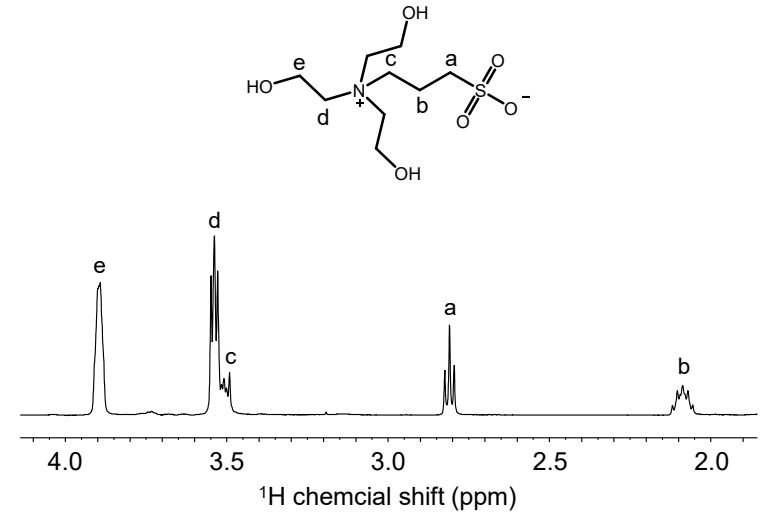


**Figure S1.** $^{1}H$ NMR spectrum of HPS in $D_2O$.

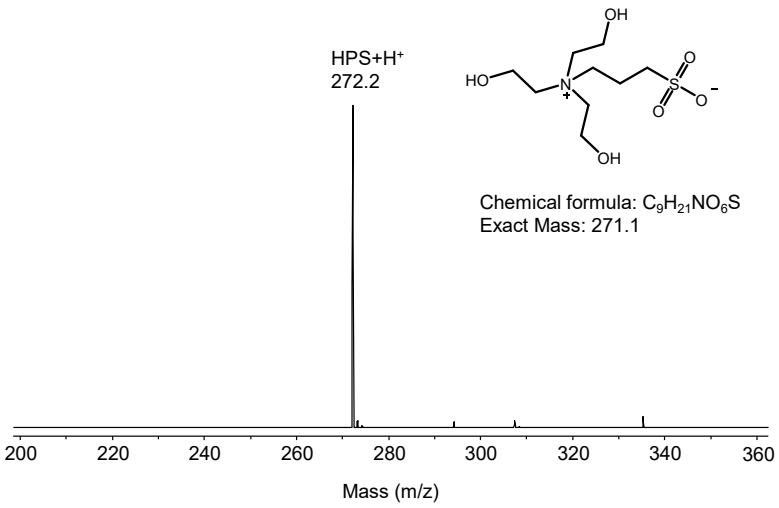


**Figure S2.** MALDI-TOF spectrum of HPS.

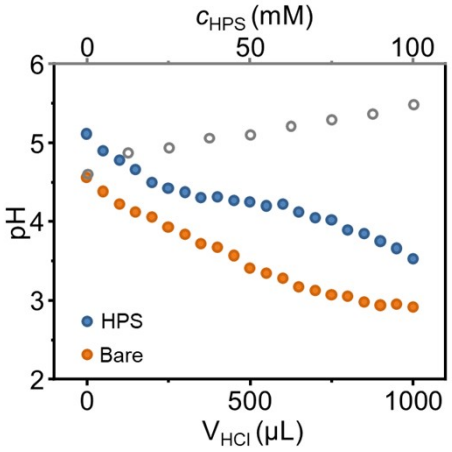


**Figure S3.** pH buffering behavior of $HPS_{50}$ versus bare electrolyte during HCl titration.

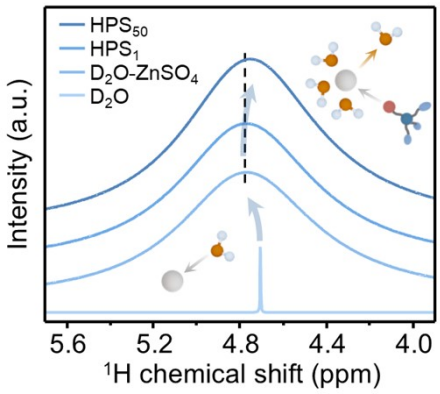


**Figure S4.** $^1$H NMR characterization of $Zn^{2+}$ solvation structure.

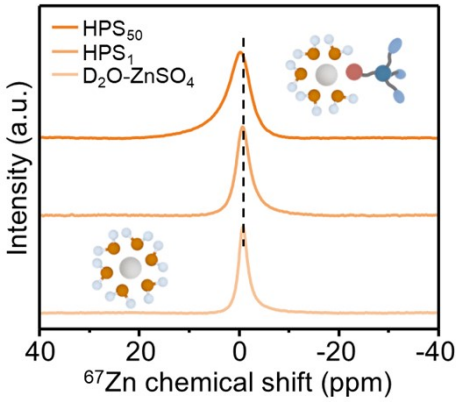


**Figure S5.** $^{67}Zn$ NMR characterization of $Zn^{2+}$ solvation structure.

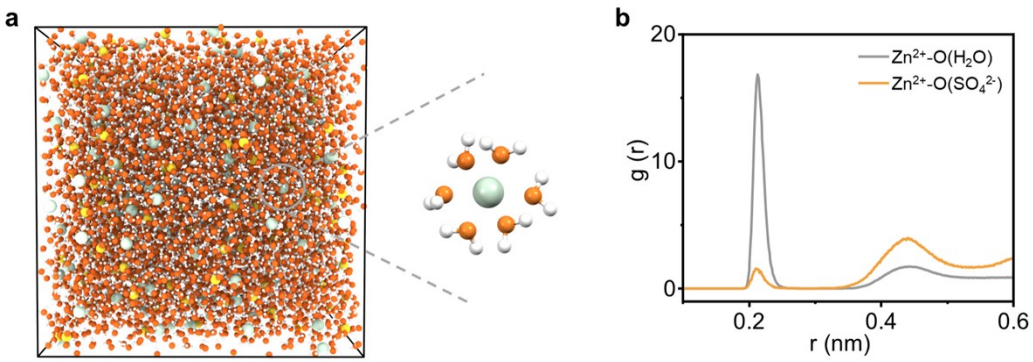


**Figure S6. a**, Molecular dynamics (MD) simulation snapshots of $Zn^{2+}$ solvation structures in the bare electrolyte. **b**, Radial distribution functions (RDFs) for bare electrolyte. The dominant solvation structure is $[Zn(H_2O)_6]^{2+}$, where $Zn^{2+}$ is coordinated by six water molecules in the primary solvation shell. Minor populations of $[Zn(H_2O)_5(SO_4)]$ contact ion pairs are also observed, characterized by direct coordination between $Zn^{2+}$ and a $SO_4^{2-}$ anion with partial displacement of one water molecule from the primary solvation shell.

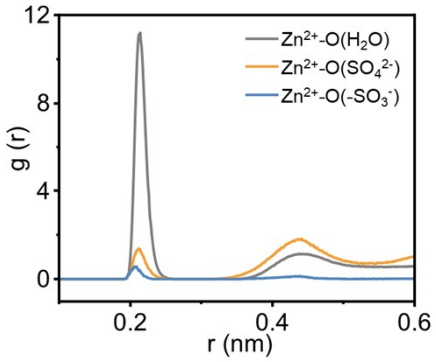


**Figure S7.** RDFs characterizing $Zn^{2+}$ coordination with oxygen-containing species in $HPS_{50}$. MD simulations were performed to probe the solvation structure of $Zn^{2+}$ in $HPS_{50}$, via RDFs of $Zn^{2+}$ with O atoms from three sources: water ($Zn^{2+}$-O($H_2O$)), sulfate anions ($Zn^{2+}$-O($SO_4^{2-}$) ), and sulfonate groups of HPS ($Zn^{2+}$-O(-$SO_3^-$) ). At short distances, the prominent peak of $Zn^{2+}$-O($H_2O$) confirms water remains in the primary solvation shell, but a distinct $Zn^{2+}$-O(-$SO_3^-$) peak at analogous distances indicates sulfonate groups of HPS competitively occupy the first coordination sphere.

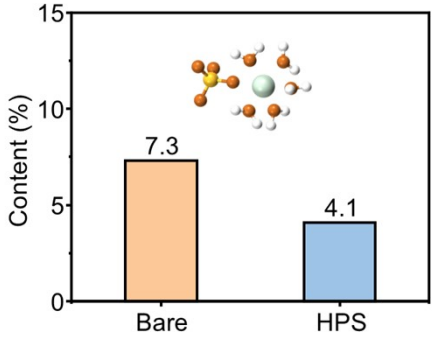


**Figure S8.** Proportion of $Zn^{2+}$-$SO_4^{2-}$ contact ion pairs in Bare and $HPS_{50}$. MD simulations were employed to quantify the percentage of $Zn^{2+}$ ions directly coordinated with $SO_4^{2-}$ anions in Bare (7.3%) and $HPS_{50}$ (4.1%). The inset schematically depicts a representative structure of such a contact ion pair, where a $SO_4^{2-}$ anion binds directly to $Zn^{2+}$ within the primary solvation shell.

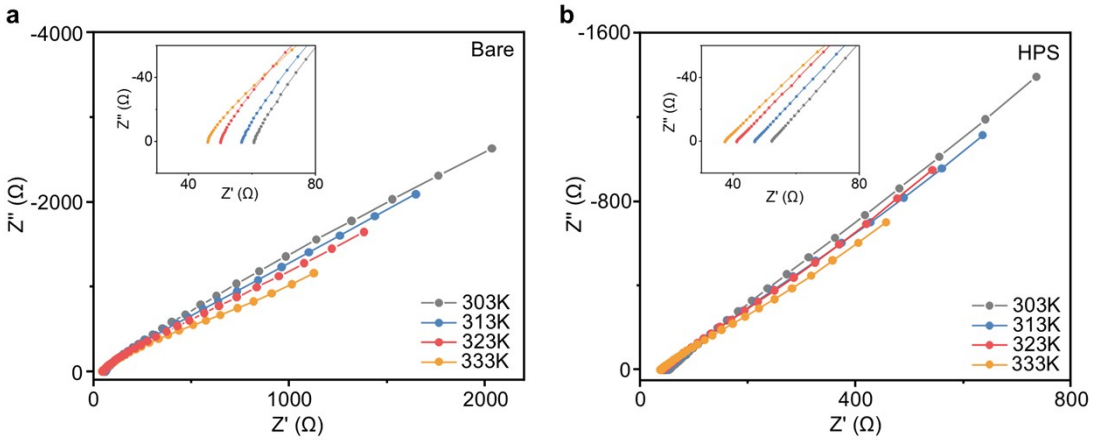


**Figure S9.** Nyquist plots of Bare and $HPS_{50}$ at 303K-333K. Insets show magnified views of the high-frequency region.

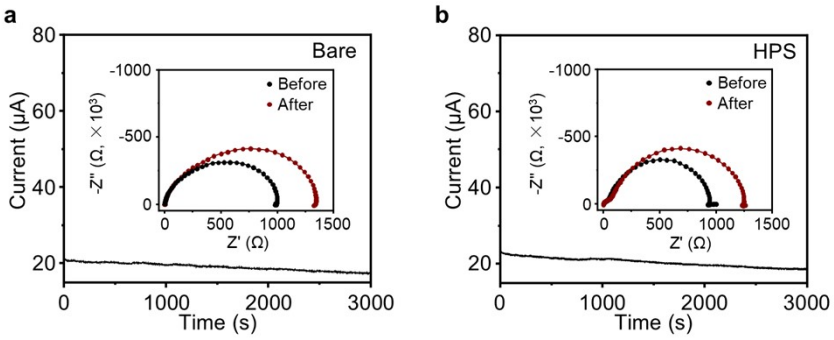


**Figure S10.** $Zn^{2+}$ transference number characterization of Bare and $HPS_{50}$ via chronoamperometry and EIS. Main panels display the time-resolved polarization current during transference number measurements. Insets present EIS Nyquist plots recorded before and after the chronoamperometric tests.

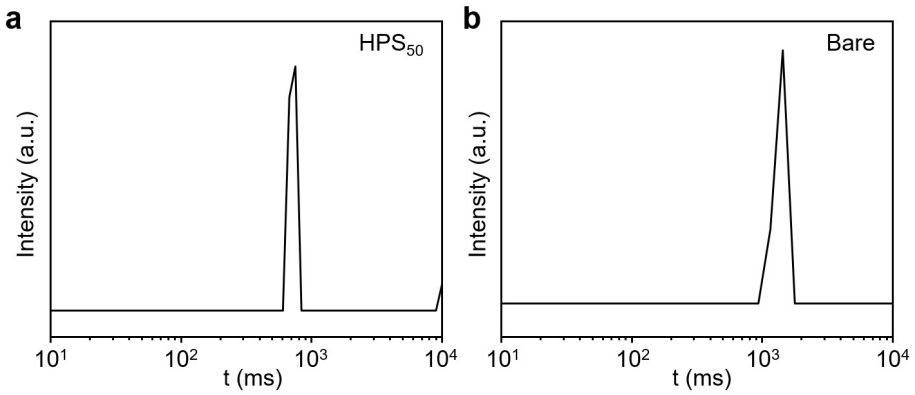


**Figure S11.** 1D $T_2$ low-field NMR spectra of (a) $HPS_{50}$ and (b) Bare electrolytes.

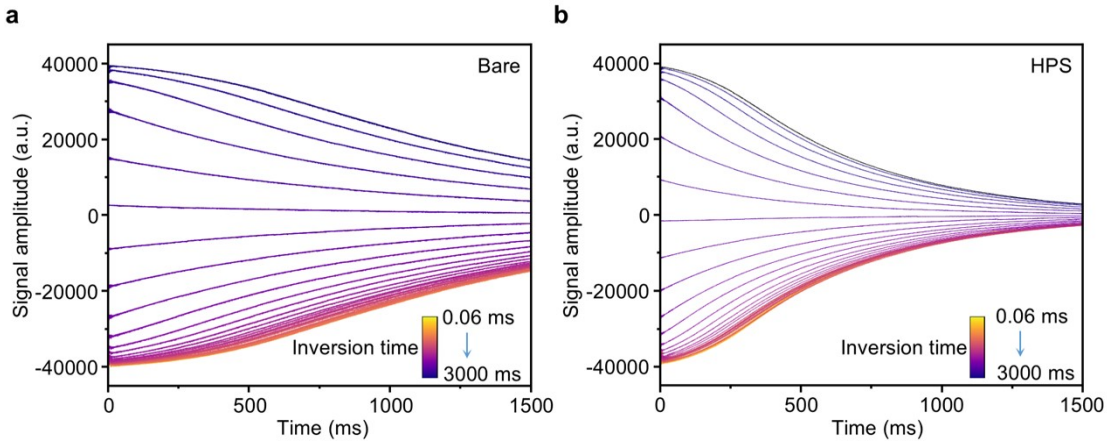


**Figure S12.** Signal amplitude as a function of time from low-field two-dimensional nuclear magnetic resonance measurements. A total of 40 measurement points were set to capture the nuclear relaxation behavior of the sample over time. Multiple curves show the decay of nuclear magnetic resonance signals under different inversion time.

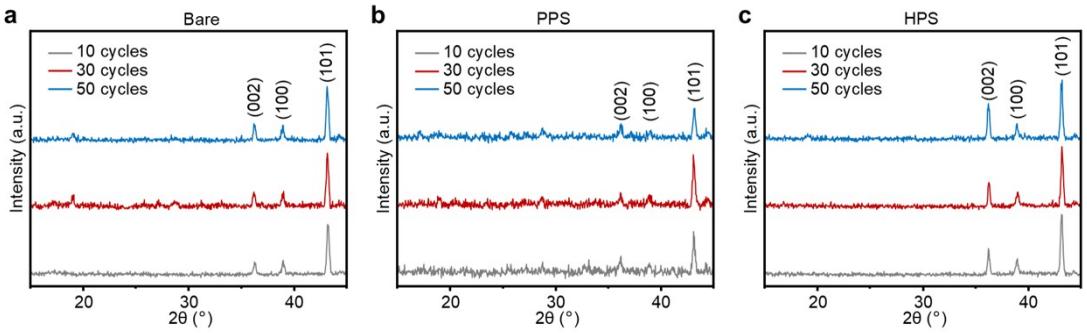


**Figure S13.** Zn deposition orientation characterized by XRD. XRD patterns of Zn deposition surfaces after 10, 30, and 50 cycles in the Bare, $PPS_{50}$, and $HPS_{50}$. Characteristic Zn diffraction peaks correspond to the (100) (~39°), (002) (~36°), and (101) (~43°) planes. For $HPS_{50}$, the (002) peak intensity increases with cycling, indicating a preferred (002) orientation. In contrast, the $PPS_{50}$ and Bare show weaker (002) peaks throughout the cycles.

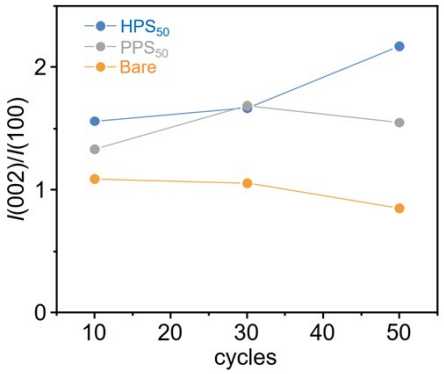


**Figure S14.** *I*(002)/*I*(100) intensity ratios of Zn anodes cycled in Bare, $PPS_{50}$, and $HPS_{50}$ electrolytes at 10, 30, and 50 cycles.

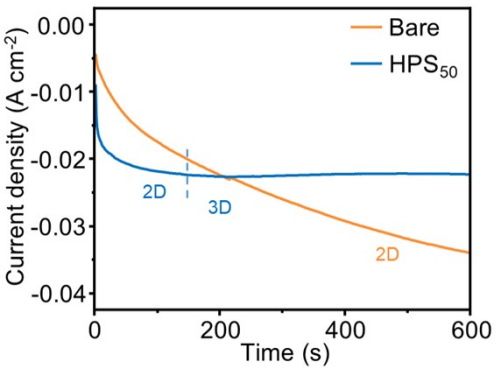


**Figure S15.** Zn deposition growth mode transition revealed by chronoamperometry. Chronoamperometric curves illustrate the current density evolution during Zn electrodeposition in the Bare and $HPS_{50}$. The curves are segmented into 2D growth and 3D growth. $HPS_{50}$ undergoes a much faster transition from 2D to 3D growth, whereas Bare sustains 2D growth for a longer duration.

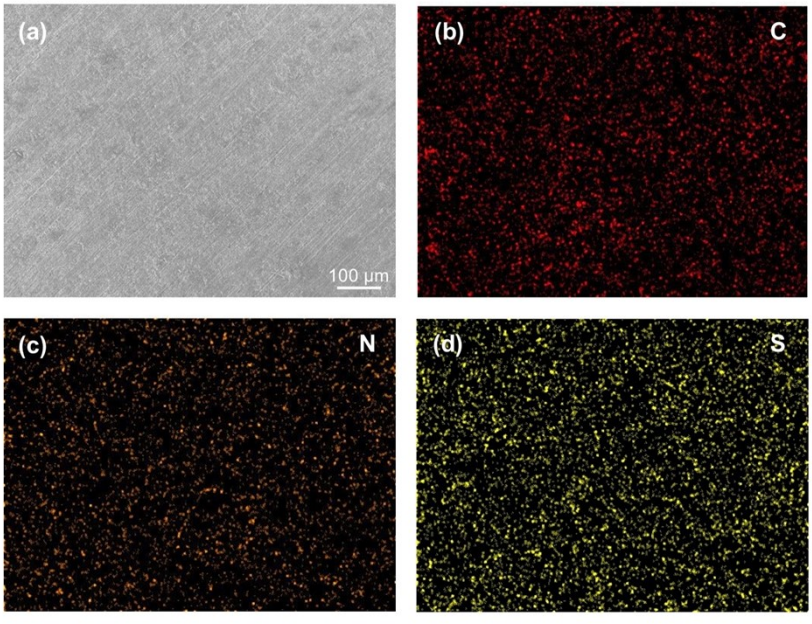


**Figure S16.** Elemental distribution confirming HPS presence at the Zn electrode interface. **a**, SEM image of the Zn electrode surface after cycling in the $HPS_1$. **b**, **c**, **d**, Corresponding elemental maps for C, N, and S. The uniform spatial overlap of N (a characteristic element of HPS) with C and S signals demonstrates the presence of HPS at the Zn/electrolyte interface.

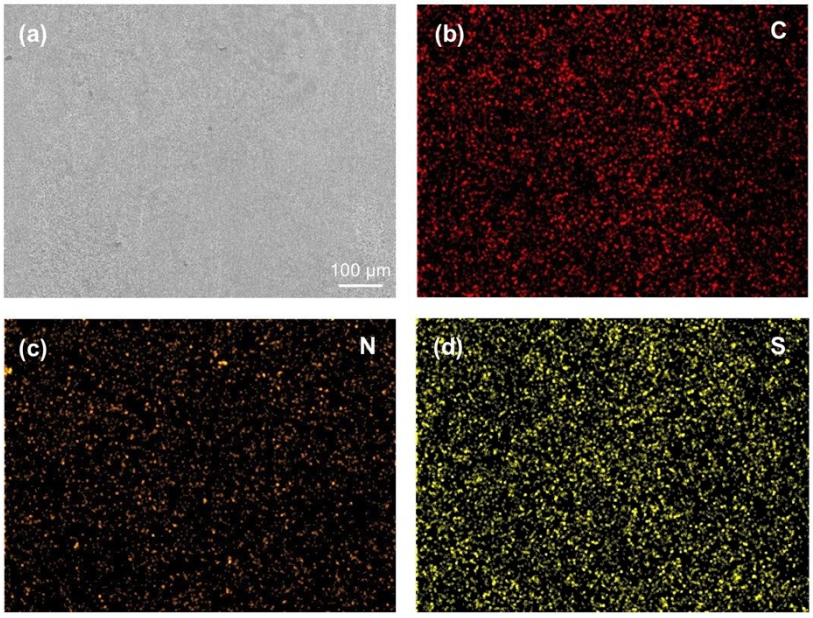


**Figure S17. a**, SEM image of the Zn electrode surface after cycling in the $HPS_{50}$. **b**, **c**, **d**, Corresponding elemental maps for C, N, and S. For the increased concentration, the uniform spatial overlap of N (a characteristic element of HPS) with C and S signals similarly demonstrates the presence of HPS at the Zn/electrolyte interface.

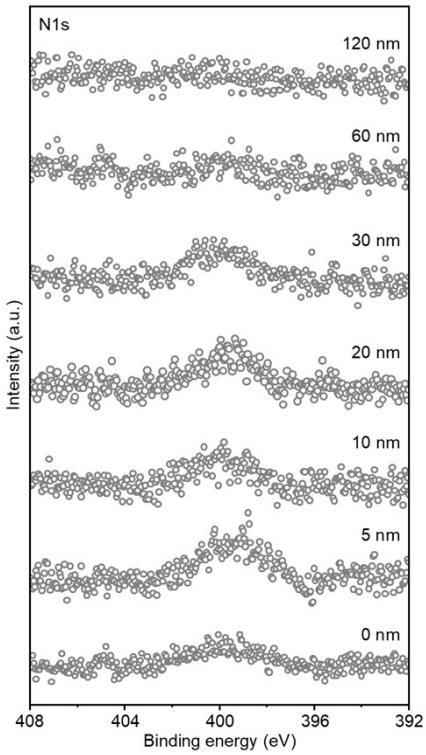


**Figure S18.** Depth-resolved XPS analysis of N 1s signal on Zn electrode. XPS depth profiling of the Zn electrode cycled in $HPS_{50}$, depicting N 1s signal intensity versus etching depth. Thet N signal (characteristic of HPS) is prominent in near-surface regions and gradually diminishes with increasing etching depth. This depth-dependent N distribution confirms HPS enrichment at the Zn/electrolyte interface, corroborating the elemental mapping in Figure S15.

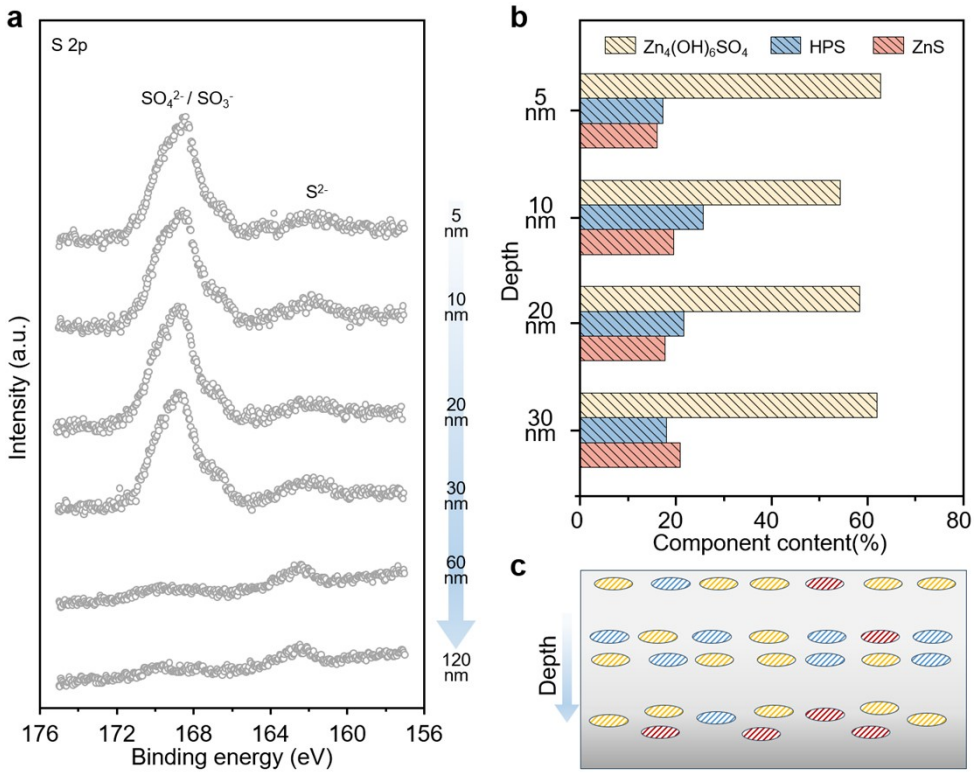


**Figure S19.** Chemical composition and depth-dependent distribution of the zwitterion-derived SEI on the Zn anode. (a) S 2p XPS depth profiling spectra of the SEI across a 120 nm depth, showing signals for $SO_4^{2-}$, $-SO_3^-$, and $S^{2-}$. (b) Quantitative depth distribution of $Zn_4(OH)_6SO_4$, HPS-derived organic species, and ZnS in the SEI. (c) Schematic illustration of the spatial distribution of SEI chemical components with increasing depth from the Zn anode surface.

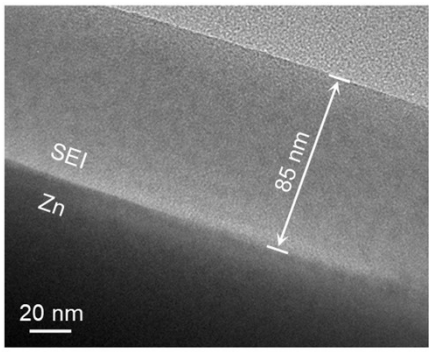


**Figure S20.** High-magnification transmission electron microscopy image of the Zn electrode after cycling in $HPS_{50}$. The dark region corresponds to the Zn, and the continuous light-contrast layer on its surface represents the solid-electrolyte interphase (scale bar: 20 nm).

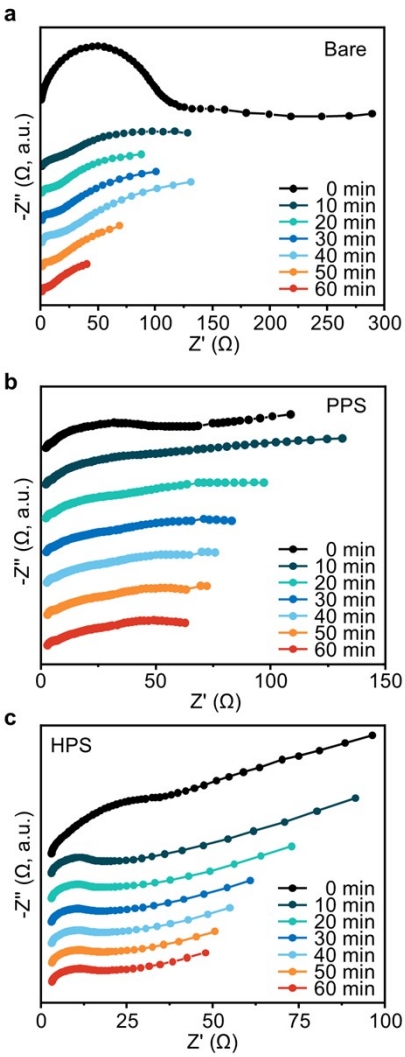


**Figure S21.** Time-resolved Nyquist plots for Zn electrodes in diverse electrolytes. EIS spectra of Zn electrodes in coin cells assembled using (a) Bare, (b) $PPS_{50}$, and (c) $HPS_{50}$. The measurements were carried out at 0, 10, 20, 30, 40, 50, and 60 minutes. These spectra capture the dynamic evolution of the Zn/electrolyte interfacial resistance during electrochemical cycling and serve as the raw data for subsequent distribution of relaxation times analysis.

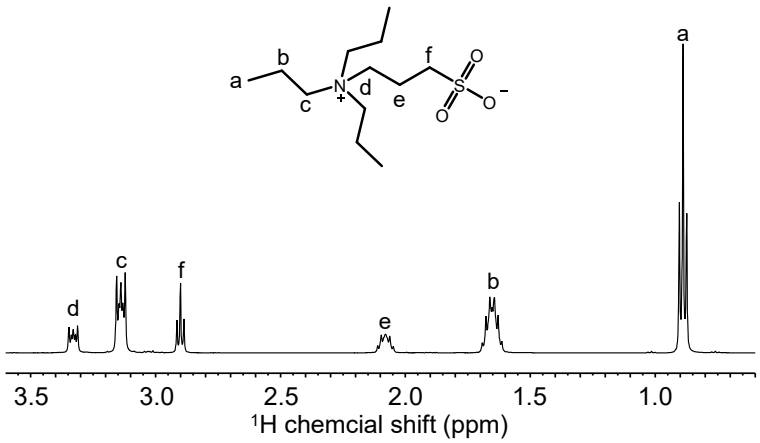


**Figure S22.** $^1$H NMR spectrum of PPS in $D_2O$.

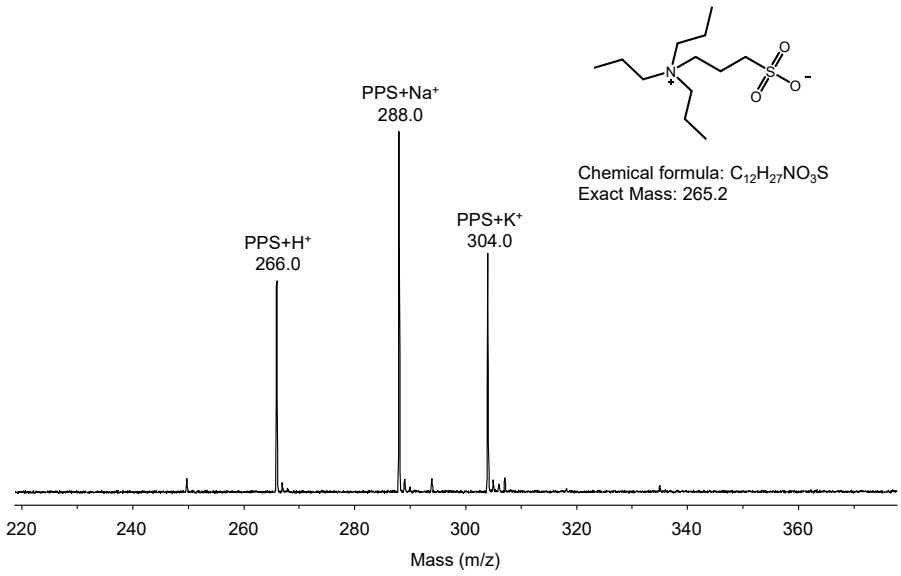


**Figure S23.** MALDI-TOF spectrum of PPS.

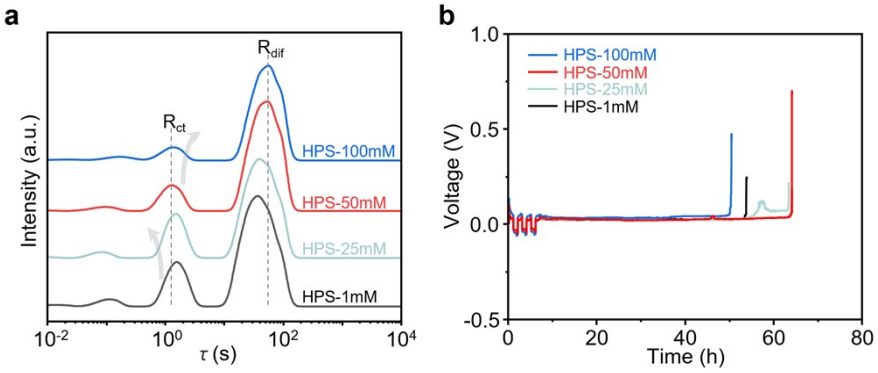


**Figure S24.** (a) Distribution of relaxation times spectra of symmetric cells with 1 mM, 25 mM, 50 mM and 100 mM HPS. (b) Continuous galvanostatic plating curves of symmetric cells with different HPS loadings.

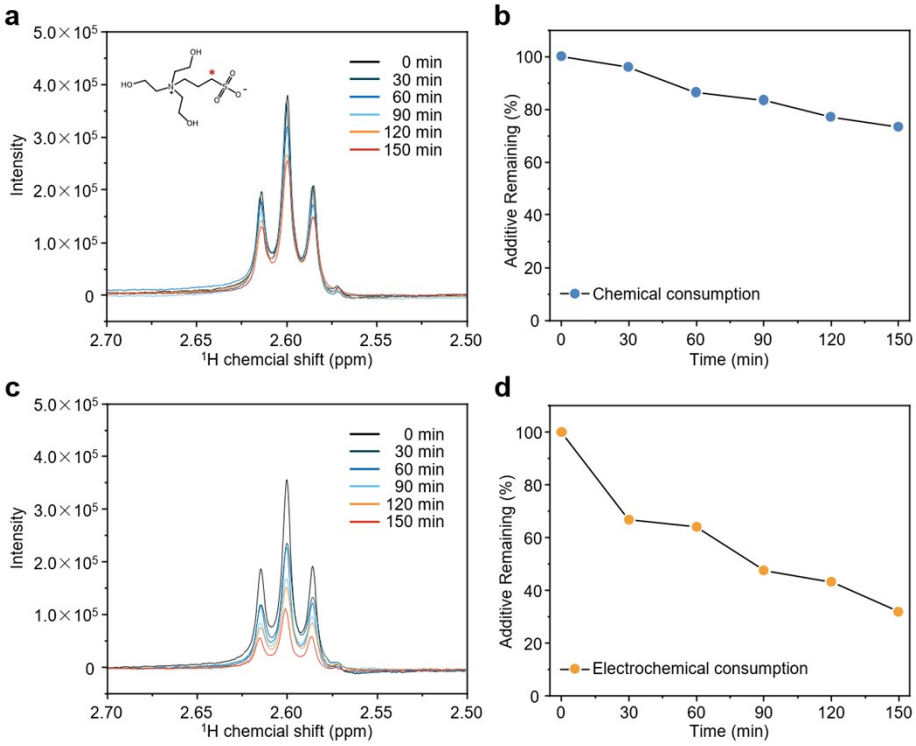


**Figure S25.** Chemical and electrochemical consumption behaviors of HPS revealed by $^{1}$H NMR characterization. (a, b) $^{1}$H NMR spectra and relative residual content of HPS in static electrolyte without applied current. (c, d) $^{1}$H NMR spectra and relative residual content of HPS in electrolyte under applied current.

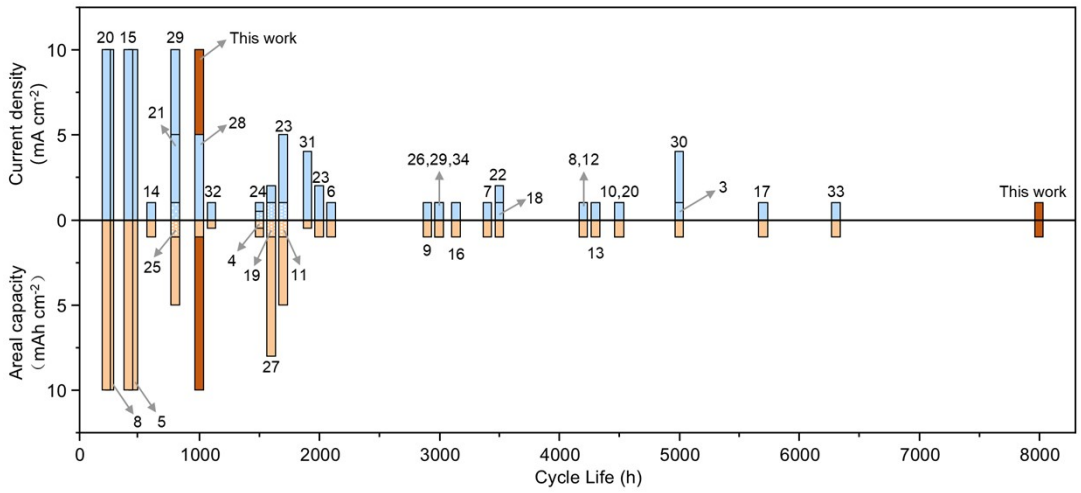


**Figure S26.** Comparison of long-term cycling performance. Zn symmetric cells cycling performance of this work versus recent works using $ZnSO_4$ electrolytes under both low (~1 mA $cm^{-2}$, ~1 mAh $cm^{-2}$) and high (~10 mA $cm^{-2}$, ~10 mAh $cm^{-2}$) current density/areal capacity conditions. Detailed references corresponding to the labeled works are provided in Table S2.

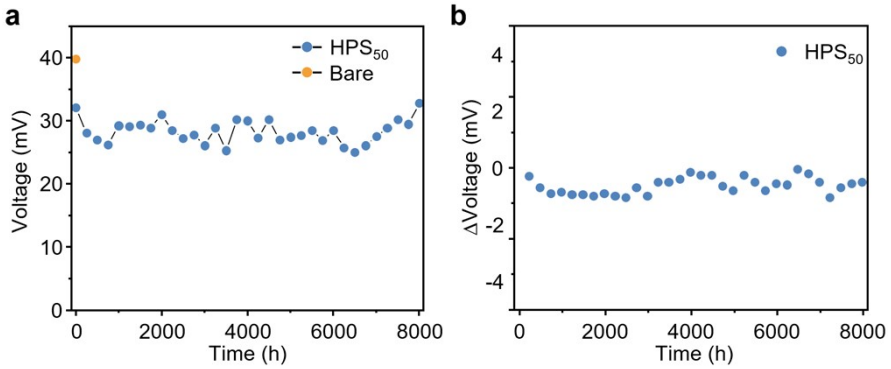


**Figure S27.** Polarization stability and deposition/stripping symmetry of Zn||Zn symmetric cells with $HPS_{50}$ electrolyte at 1 mA $cm^{-2}$, 1 mAh $cm^{-2}$ for 8000 h. (a) Charging polarization voltage recorded every 250 h. (b) Δ Voltage (charging polarization−discharging polarization) during cycling.

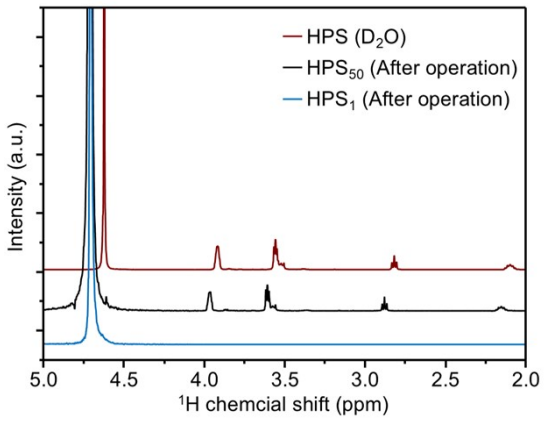


**Figure S28.** $^{1}$H NMR spectra comparing HPS dissolved in $D_2O$ and electrolyte extracted from a Zn symmetric cell operated for 240 hours using $HPS_1$ and $HPS_{50}$ (the extracted electrolytes were diluted with $D_2O$ prior to analysis). The characteristic peaks of HPS remain detectable in the electrolyte extracted from the $HPS_{50}$ cell, confirming that a significant fraction of HPS molecules is retained in the electrolyte and maintains its structural integrity during operation. In contrast, the spectrum of the electrolyte from the $HPS_1$ cell shows no discernible HPS-derived signals. This observation provides direct experimental evidence for our proposed concentration-dependent dual functionality. At a low concentration ($HPS_1$), the additive is predominantly consumed in forming a protective SEI on the zinc anode, leaving no free molecules in the bulk electrolyte. At a higher concentration ($HPS_{50}$), the zwitterion is supplied in sufficient quantity to simultaneously construct a stable interface and remain in the electrolyte to participate in bulk ion solvation and transport regulation, which is crucial for the exceptional long-term stability observed.

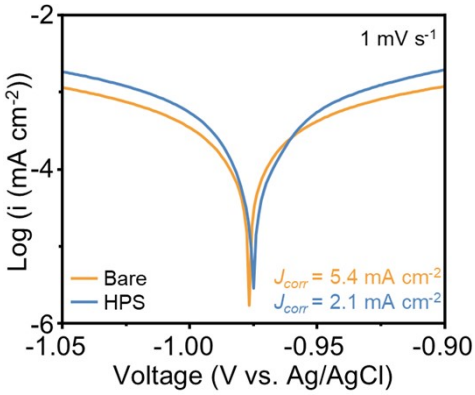


**Figure S29.** Tafel plots of Zn electrodes in Bare and $HPS_{50}$ were recorded at a scan rate of 1 mV $s^{-1}$ (vs. Ag/AgCl). $HPS_{50}$ exhibits a significantly lower corrosion current density ($J_{corr}$ = 2.1 mA $cm^{-2}$) compared to Bare ($J_{corr}$ = 5.4 mA $cm^{-2}$), indicating enhanced resistance to Zn corrosion.

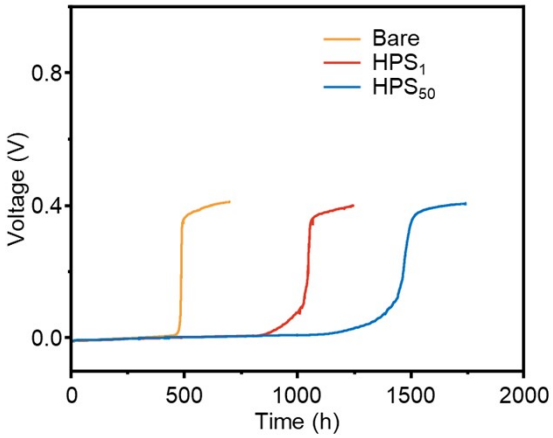


**Figure S30.** Open-circuit voltage (OCV) evolution of Zn–Cu half-cells during open-circuit hold after Zn plating. Zn–Cu half-cells were fabricated with Bare, $HPS_1$, and $HPS_{50}$. After galvanostatically plating Zn on Cu at 1 mA $cm^{-2}$ to 2 mAh $cm^{-2}$, OCV was recorded during subsequent open-circuit hold. The $HPS_{50}$ maintains OCV near 0 V for the longest duration, indicating minimal corrosion of the plated Zn layer. In contrast, the Bare and $HPS_1$ exhibits a rapid OCV rise due to severe Zn corrosion.

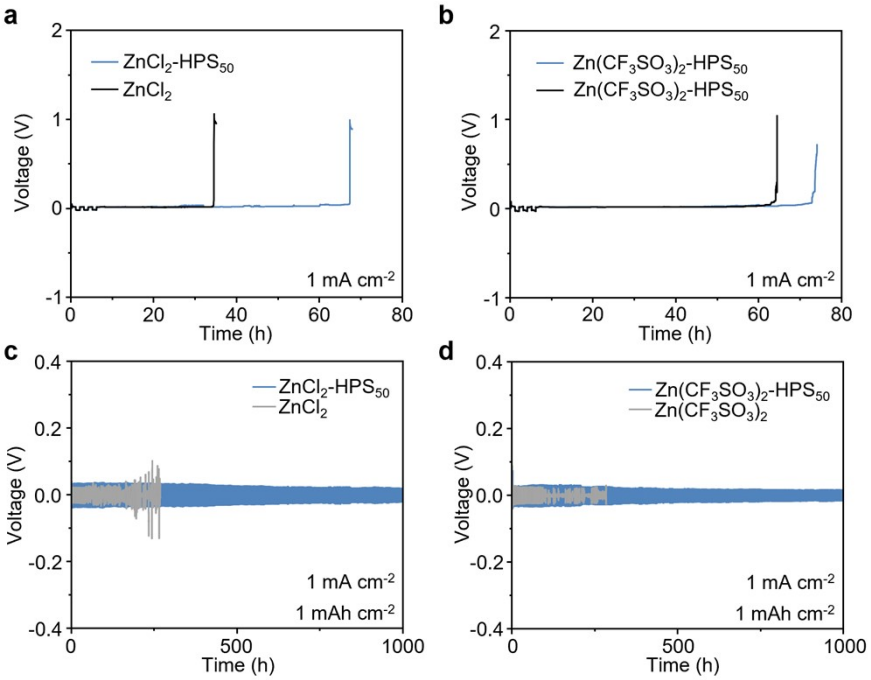


**Figure S31.** Zn||Zn symmetric cell performance in $ZnCl_2$ and $Zn(CF_3SO_3)_2$ electrolytes with and without 50 mM HPS at a current density of 1 mA $cm^{-2}$. (a, b) Continuous plating tests comparing the failure time of cells with bare electrolyte and HPS-containing electrolyte. (c, d) Long-term galvanostatic cycling stability of cells with bare electrolyte and HPS-containing electrolyte over the tested duration.

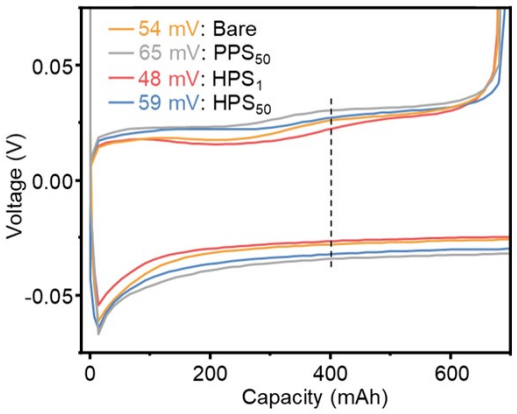


**Figure S32.** Voltage hysteresis analysis of Zn–Cu half-cells with varied electrolytes. Galvanostatic charge–discharge curves of Zn–Cu half-cells using Bare, $HPS_1$, $HPS_{50}$, and $PPS_{50}$, measured under the condition of 1 mA $cm^{-2}$ and 1 mAh $cm^{-2}$ areal capacity. Voltage hysteresis (ΔV) was measured at 400 mAh, where the HPS system exhibits a smaller ΔV compared to Bare and $PPS_{50}$, indicating improved Zn deposition/dissolution kinetics at the electrode interface.

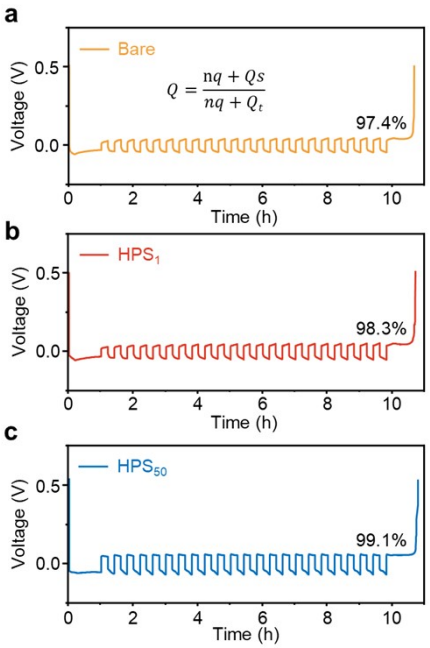


**Figure S33.** Coulombic efficiency (CE) profiles of Zn–Cu half-cells with varied electrolytes. Galvanostatic cycling curves of Zn–Cu half-cells using (a) Bare, (b) $HPS_1$, and (c) $HPS_{50}$. The $HPS_{50}$ exhibits the highest CE (99.1%), followed by $HPS_1$ (98.3%) and Bare (97.4%), indicating that the presence of HPS both at the interface and within the bulk electrolyte is crucial for achieving highly reversible Zn deposition/dissolution.

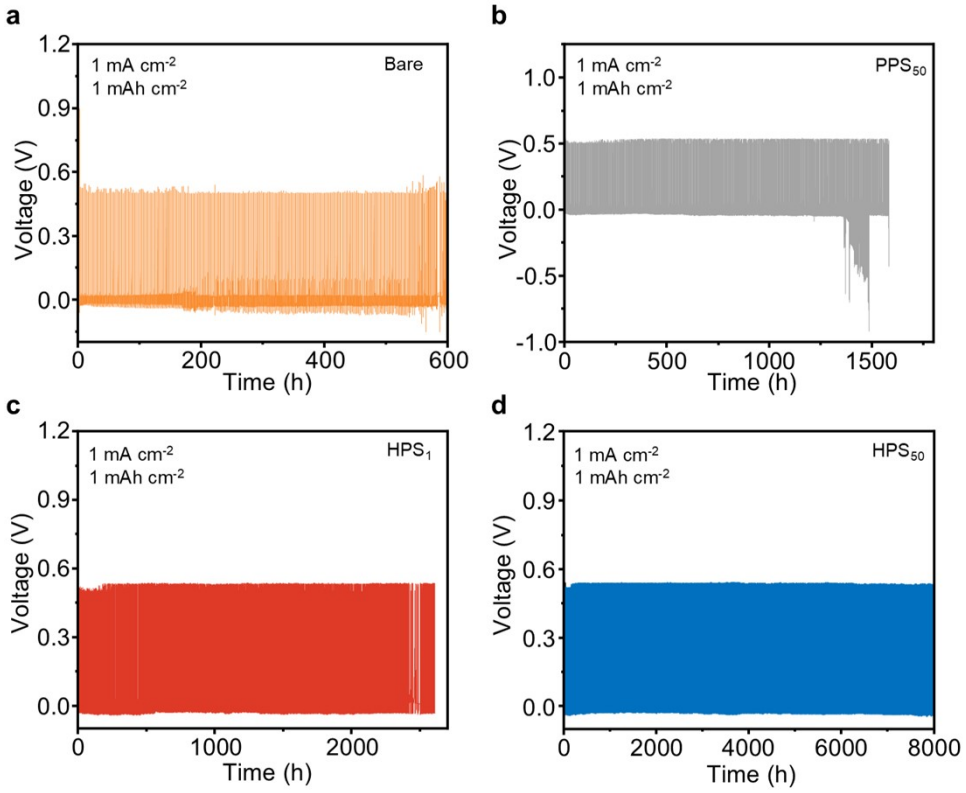


**Figure S34.** Long-term voltage-time profiles of Zn–Cu half-cells with varied electrolytes. Galvanostatic cycling voltage profiles of Zn–Cu half-cells using (a) Bare, (b) $PPS_{50}$, (c) $HPS_1$, and (d) $HPS_{50}$, operated at 1 mA $cm^{-2}$ with 1 mAh $cm^{-2}$ areal capacity. The $HPS_{50}$-based cell exhibits the most stable voltage plateau and longest cycling lifespan.

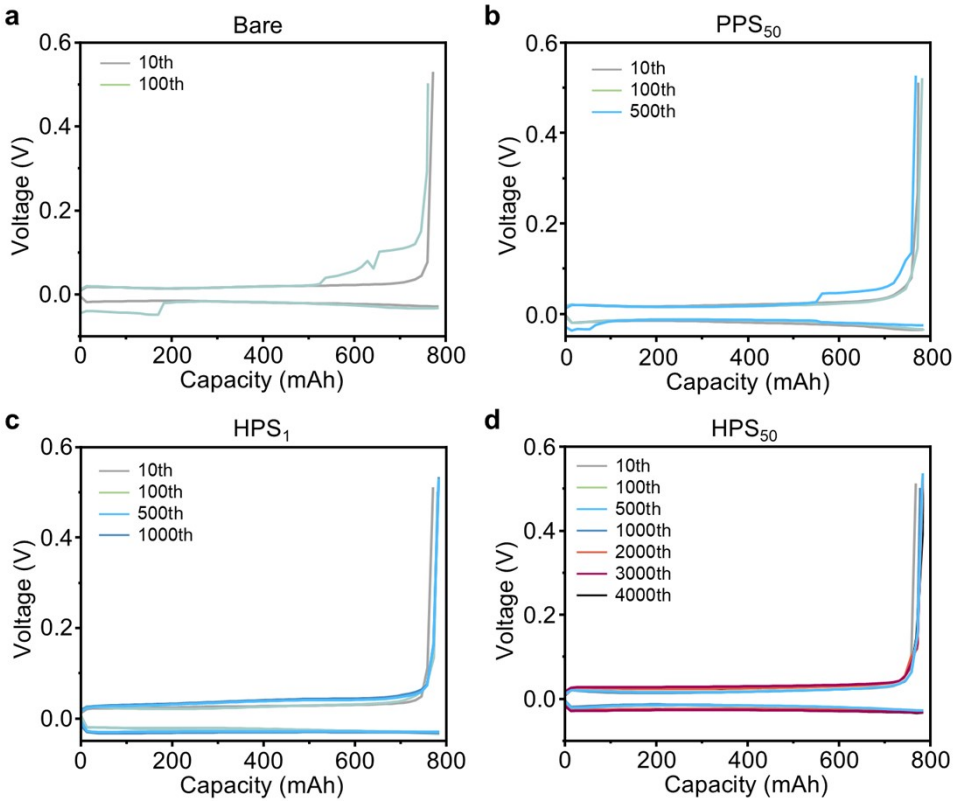


**Figure S35.** Voltage-capacity profiles of Zn–Cu half-cells during long-term cycling with different electrolytes. Voltage-capacity curves of Zn-Cu half-cells using (a) Bare, (b) $PPS_{50}$, (c) $HPS_1$, and (d) $HPS_{50}$ are shown. The tests were conducted at a current density of 1 mA $cm^{-2}$ and 1 mAh $cm^{-2}$. Curves for different cycle numbers (10th, 100th, 500th, 1000th, 2000th, $3000^{th}$, $4000^{th}$ as labeled) are presented to illustrate the cycling stability. $HPS_{50}$ exhibits the most stable voltage-capacity behavior across a large number of cycles.

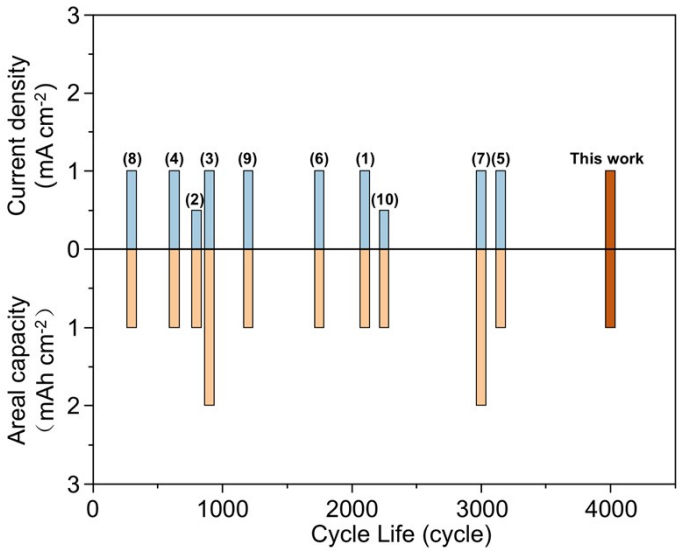


**Figure S36.** Comparison of long-term cycling performance. Zn–Cu half-cells cycling performance of this work versus recent works using $ZnSO_4$ electrolytes at ~1 mA $cm^{-2}$ and ~1 mAh $cm^{-2}$. Detailed references corresponding to the labeled works are provided in Table S3.

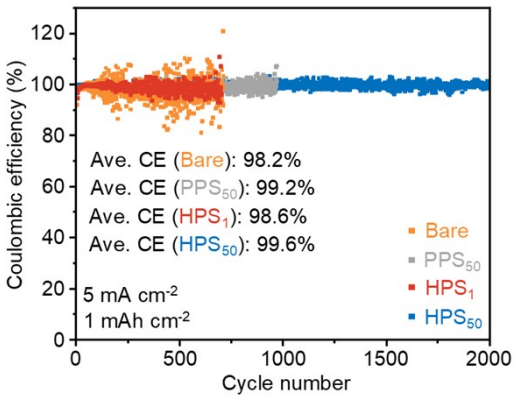


**Figure S37.** Long-term cycling Coulombic efficiency (CE) of Zn–Cu half-cells with different electrolytes. CE profiles of Zn–Cu half-cells using Bare, $PPS_{50}$, $HPS_1$, and $HPS_{50}$ during long-term galvanostatic cycling at a current density of 5 mA $cm^{-2}$ and 1 mAh $cm^{-2}$ are shown. $HPS_{50}$ exhibits the highest and most stable CE over 2000 cycles.

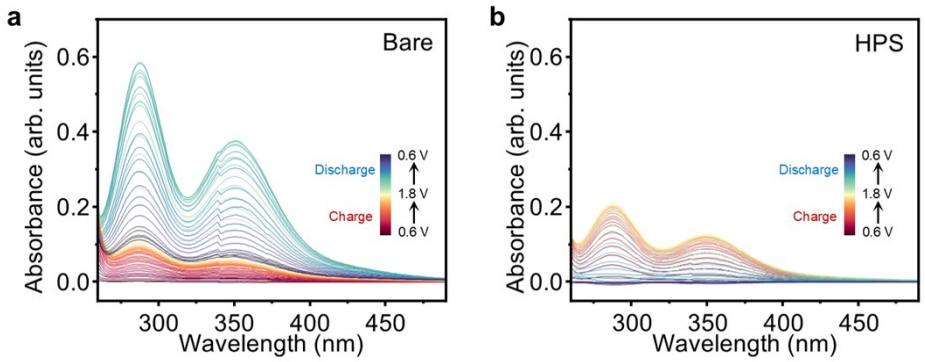


**Figure S38.** *In situ* UV-vis spectra of full-cells during charge-discharge processes. *In situ* UV-vis absorption spectra of full-cells using (a) Bare and (b) $HPS_{50}$ are shown. The spectra were recorded during the process of charging the cells from 0.6 V to 1.8 V and then discharging back to 0.6 V. The color-coded lines represent the spectral changes at different voltage states during charge and discharge.

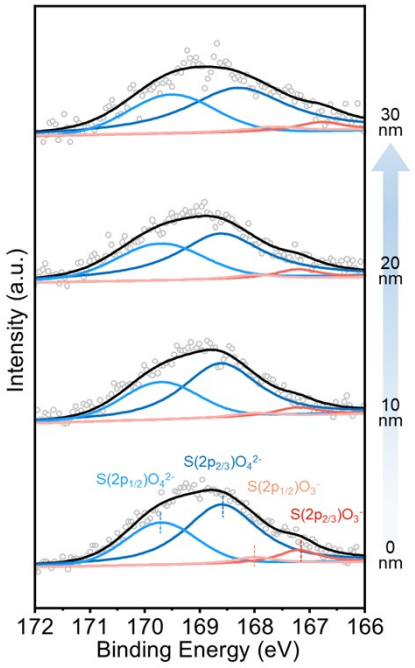


**Figure S39.** XPS of S 2p orbitals at different etching depths on the cathode-side of full-cells. The spectra are deconvoluted into components corresponding to different sulfur-containing species, such as $S(2p_{1/2})O_4^{2-}$, $S(2p_{2/3})O_4^{2-}$, $-S(2p_{1/2})O_3^{-}$, and $-S(2p_{2/3})O_3^{-}$.

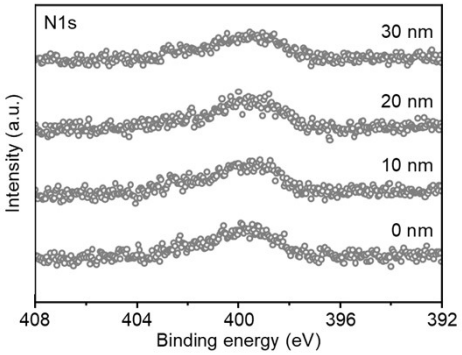


**Figure S40.** XPS N1s spectra at different etching depths on the cathode-side of full-cells. As N is a characteristic element of HPS, the presence of N-related signals at different depths indicates the existence of HPS-containing components in the cathode electrolyte interphase.

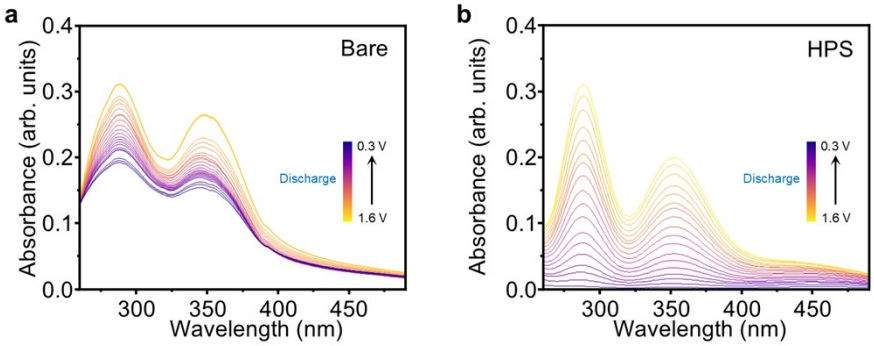


**Figure S41.** *In situ* UV-vis absorption spectra of full cells with (a) Bare and (b) $HPS_{50}$. Cathodes with identical iodine loadings (5.0 mg $cm^{-2}$) were cycled 10 times using Bare and $HPS_{50}$, respectively. The electrolyte was subsequently replaced with a 2 M $ZnSO_4$ solution containing $I_3^-$ (from $ZnI_2$ + $I_2$) at 5 mg $mL^{-1}$ to ensure consistent initial iodine content in the electrolyte, and the discharge process was recorded. Lines of different colors represent spectral changes at various voltage states during discharge, ranging from 1.6 V to 0.3 V.

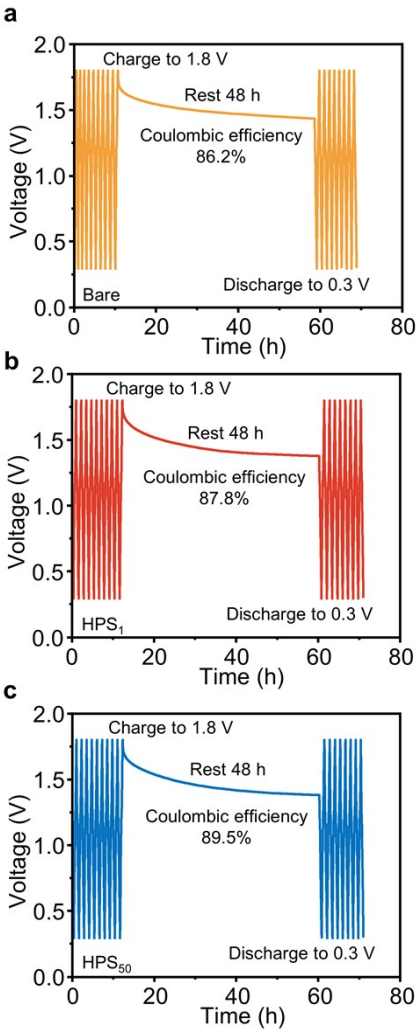


**Figure S42.** Self-discharge performance of full-cells with different electrolytes. The cells were charged to 1.8 V, rested for 48 h, and then discharged to 0.3 V. The Coulombic efficiency during this process is indicated for each electrolyte: 86.2% for (a) Bare, 87.8% for (b) $HPS_1$, and 89.5% for (c) $HPS_{50}$. $HPS_{50}$ exhibits the best self-discharge performance.

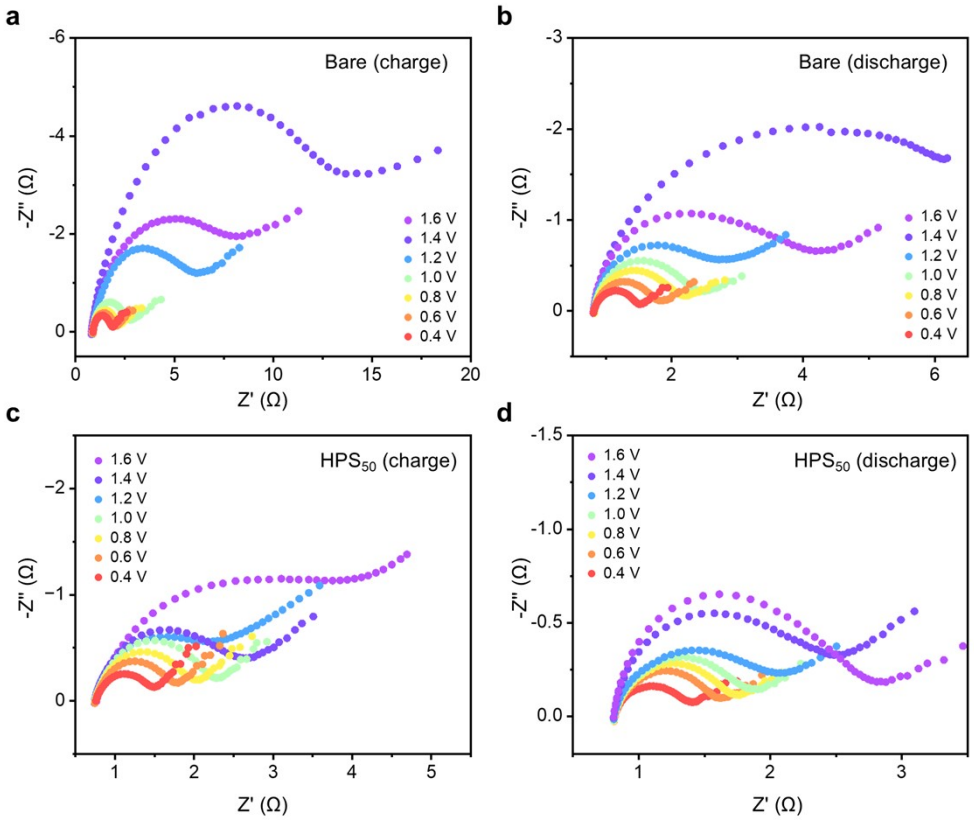


**Figure S43** Comparative Nyquist plots at different voltages. The electrochemical impedance spectra were collected for Bare (a, b) and the $HPS_{50}$ (c, d) during charging (a, c) and discharging (b, d) processes, respectively, to elucidate the effect of the HPS additive on the interfacial impedance under operational conditions.

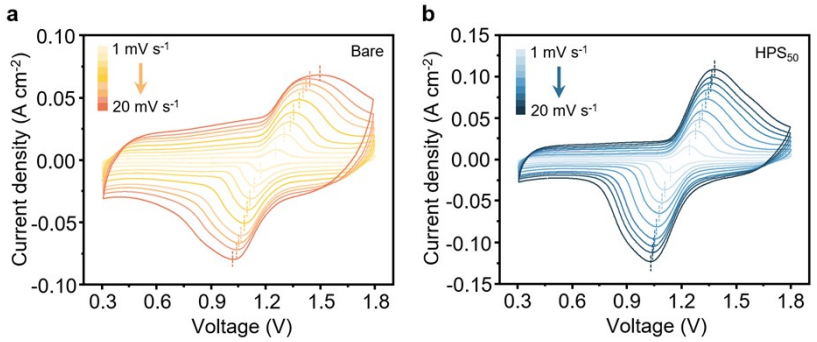


**Figure S44.** Cyclic voltammetry (CV) curves of Zn–$I_2$ full cells measured at scan rates from 1 to 20 mV $s^{-1}$. The CV profiles of cells with (a) Bare and (b) $HPS_{50}$ show distinct features. Bare exhibits broad and poorly resolved redox peaks, suggesting significant polarization and sluggish reaction kinetics, which may be attributed to uncontrolled iodine species dissolution and shuttling, as well as inefficient charge transfer. In contrast, the CV curves of $HPS_{50}$ display more symmetric redox peaks, indicating improved reversibility of the iodine redox reactions. This enhancement is due to the effective suppression of polyiodide shuttling by HPS-mediated interfacial anchoring, which maintains electrochemically active $I_3^-$ concentrations and facilitates efficient charge transfer. The reduced polarization and improved peak definition further confirm the role of HPS in stabilizing the electrode-electrolyte interface and optimizing the local electrochemical environment.

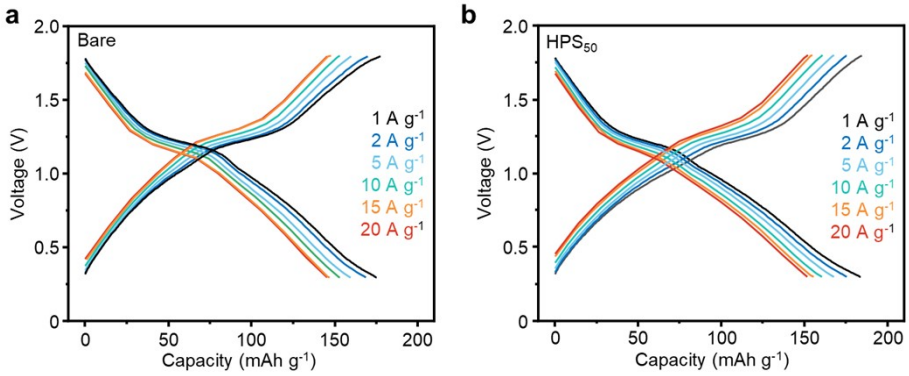


**Figure S45.** Rate-performance capacity-voltage curves of full-cells. Capacity-voltage curves of full-cells using (a) Bare and (b) $HPS_{50}$ are presented under different current rates (1 A $g^{-1}$, 2 A $g^{-1}$, 5 A $g^{-1}$, 10 A $g^{-1}$, 15 A $g^{-1}$, 20 A $g^{-1}$).

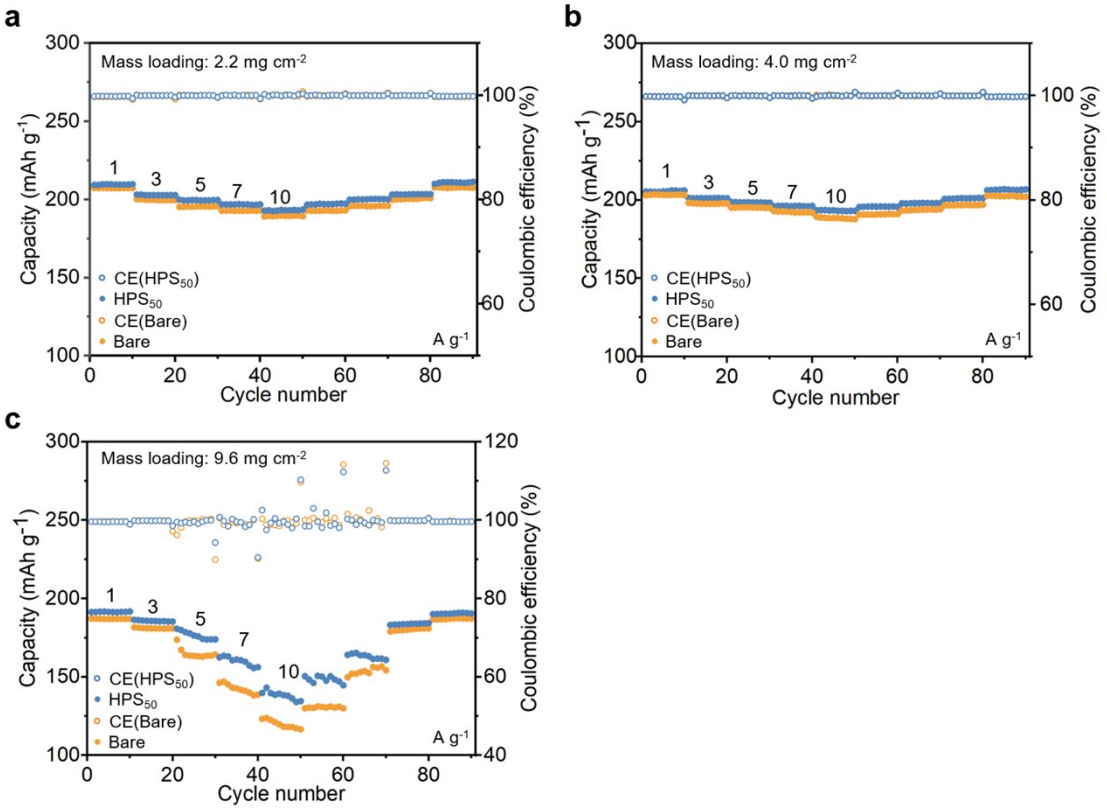


**Figure S46.** Rate capability of Zn–$I_2$ coin cells with different areal iodine loadings in bare and 50 mM HPS-modified electrolytes. (a) 2.2 mg $cm^{-2}$, (b) 4.0 mg $cm^{-2}$, (c) 9.6 mg $cm^{-2}$.

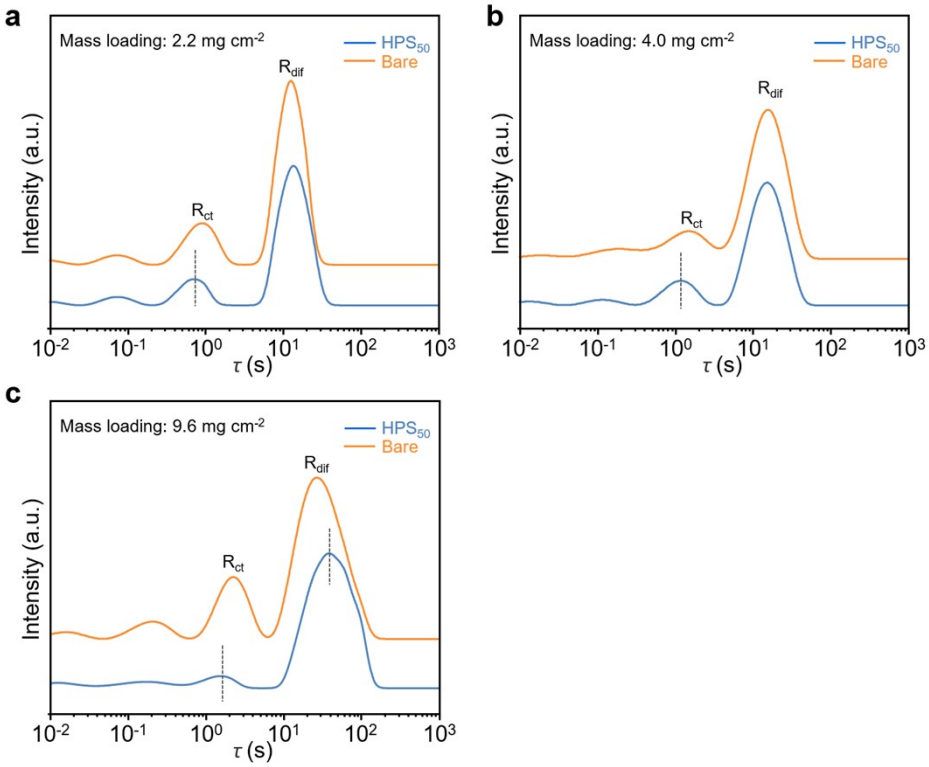


**Figure S47.** DRT analysis of Zn–$I_2$ coin cells with different areal iodine loadings in bare and 50 mM HPS-modified electrolytes. (a) 2.2 mg $cm^{-2}$, (b) 4.0 mg $cm^{-2}$, (c) 9.6 mg $cm^{-2}$, deconvolving charge transfer resistance ($R_{ct}$) and diffusion resistance ($R_{diff}$) at the cathode interface. To understand the origin of these kinetic limitations, we turned to distribution of relaxation times analysis of the cells at different loadings. At 2.2 and 4.0 mg $cm^{-2}$, the HPS-modified system exhibits a shorter relaxation time associated with charge-transfer resistance relative to the bare system, confirming that the cation–hydroxyl interaction primarily facilitates interfacial charge transfer. At 9.6 mg $cm^{-2}$, however, the relaxation time corresponding to diffusion resistance becomes significantly broadened in the HPS-modified cell and actually exceeds that of the bare cell, even though the charge-transfer relaxation time remains shorter. This pattern suggests that under ultra-high loading, the dominant bottleneck shifts from interfacial kinetics to bulk mass transport of polyiodide species within the cathode, a limitation that the trapping mechanism cannot fully mitigate at very high rates.

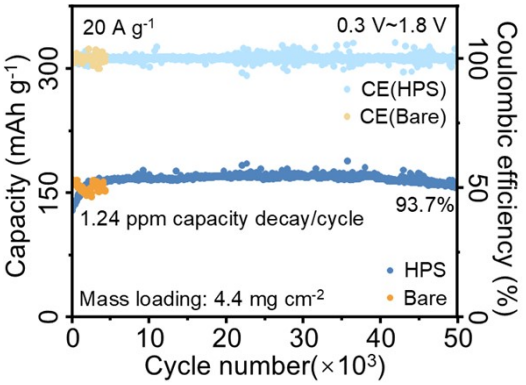


**Figure S48.** Cycling performance comparison of Bare and $HPS_{50}$ in Zn–$I_2$ coin cells under conditions of 20 A $g^{-1}$ within a 0.3–1.8 V voltage window.

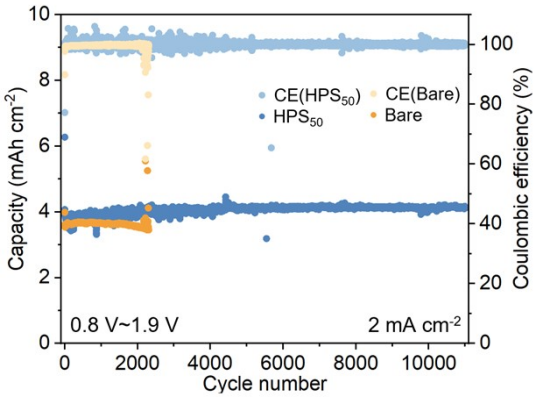


**Figure S49.** Cycling performance of static Zn–$Br_2$ batteries with bare electrolyte and electrolyte containing 50 mM HPS.

## 3. Supplementary Tables

**Table S1.** The conductivities of $HPS_{50}$ and Bare.

| Conductivity\Sample | $HPS_{50}$ | Bare |
|---|---|---|
| 303 K | 0.0436 S $cm^{-1}$ | 0.04 S $cm^{-1}$ |
| 308 K | 0.0439 S $cm^{-1}$ | 0.0412 S $cm^{-1}$ |
| 313 K | 0.0452 S $cm^{-1}$ | 0.0431 S $cm^{-1}$ |
| 318 K | 0.0474 S $cm^{-1}$ | 0.0453 S $cm^{-1}$ |
| 323 K | 0.0488 S $cm^{-1}$ | 0.0475 S $cm^{-1}$ |

**Table S2.** Performance comparison among Zn symmetric cells.

| No. | Current density（mA $cm^{-2}$) | Areal capacity（mAh $cm^{-2}$） | Cycle life (h) | Reference |
|---|---|---|---|---|
| 1 | 1 | 1 | 8000 | This work |
| 2 | 10 | 10 | 1000 | This work |
| 3 | 1 | 1 | 5000 | *J. Am. Chem. Soc*. **2025**, *147*, 9294−9303. |
| 4 | 0.5 | 0.5 | 1500 | *Angew. Chem. Int. Ed.* **2025**, *64*, e202424642. |
| 5 | 10 | 10 | 450 | *J. Am. Chem. Soc*. **2025**, *147*, 23331−23338. |
| 6 | 1 | 1 | 2100 | *Angew. Chem. Int. Ed*. **2025**, *64*, e202424095. |
| 7 | 1 | 1 | 3400 | *Adv. Mater*. **2025**, *37*, 2420079. |
| 8 | 1<br>10 | 1<br>10 | 4200<br>250 | *Angew. Chem. Int. Ed.* **2025**, *64*, e202414166. |
| 9 | 1 | 1 | 2900 | *Angew. Chem. Int. Ed.* **2025**, *64*, e202423326. |
| 10 | 1 | 1 | 4500 | *Adv. Mater*. **2025**, *37*, 2420221. |
| 11 | 1 | 1 | 1700 | *Adv. Energy Mater.* **2025**, *15*, 2404450. |
| 12 | 1 | 1 | 4200 | *Energy Environ. Sci.*, **2025**, *18*, 4800–4810. |
| 13 | 1 | 1 | 4300 | *Adv. Funct. Mater.* **2025**, *35*, 2415107. |

| | | | | |
|---|---|---|---|---|
| 14 | 1 | 1 | 600 | *Energy Environ. Sci*. **2025**, *18*, 2973−2984. |
| 15 | 10 | 10 | 410 | *Adv. Funct. Mater.* **2025**, *35*, 2415107. |
| 16 | 1 | 1 | 3140 | *J. Am. Chem. Soc.* **2024***, 146,* 30998−31011. |
| 17 | 1 | 1 | 5700 | *Angew. Chem. Int. Ed*. **2024**, *63*, e202410422. |
| 18 | 1 | 1 | 3500 | *Nat. Commun*. **2024**, *15*, 9702. |
| 19 | 1 | 1 | 1600 | *Adv. Energy Mater.* **2024**, *14*, 2400353. |
| 20 | 1<br>10 | 1<br>10 | 4500<br>225 | *Chem. Sci.* **2024**, *15*, 1488–1497. |
| 21 | 5 | 1 | 800 | *Adv. Funct. Mater.* **2024**, *34*, 2402484. |
| 22 | 2 | 1 | 3500 | *Adv. Funct. Mater.* **2024**, *34*, 2401537. |
| 23 | 2<br>5 | 1<br>5 | 2000<br>1700 | *Energy Environ. Sci.* **2024**, *17*, 2888–2896. |
| 24 | 1 | 1 | 1500 | *J. Am. Chem. Soc*. **2023**, *145*, 15776−15787. |
| 25 | 1 | 1 | 800 | *J. Am. Chem. Soc.* **2023**, *145*, 20109−20120. |
| 26 | 1 | 1 | 3000 | *Angew. Chem. Int. Ed.* **2023**, *62*, e202302701. |
| 27 | 2 | 8 | 1600 | *Nat. Commun.* **2023**, *14*, 3067. |
| 28 | 5 | 1 | 1000 | *Angew. Chem. Int. Ed.* **2023**, *62*, e202218872. |
| 29 | 1<br>10 | 1<br>5 | 3000<br>800 | *Adv. Mater.* **2023***, 35,* 2306531. |
| 30 | 4 | 1 | 5000 | *ACS Nano* **2023**, *17*, 23181–23193. |
| 31 | 4 | 0.5 | 1900 | *Angew. Chem. Int. Ed.* **2023**, *62*, e202212695. |
| 32 | 1 | 0.5 | 1100 | *Adv. Funct. Mater.* **2023**, *34*, 2214538. |
| 33 | 1 | 1 | 6308 | *Energy Environ. Sci.* **2023**, *16*, 2684–2695. |
| 34 | 1 | 1 | 3000 | *Adv. Energy Mater.* **2023**, *13*, 2302676. |

**Table S3.** Performance comparison among Zn||Cu half-cells.

| No. | Current density（mA $cm^{-2}$） | Areal capacity（mAh $cm^{-2}$） | Cycle life (cycle) | Reference |
|---|---|---|---|---|
| | 1 | 1 | 4000 | This work |
| 1 | 1 | 1 | 2100 | *J. Am. Chem. Soc.* **2025**, *147*, 8523−85331 |
| 2 | 1 | 0.5 | 800 | *Adv. Mater*. **2025**, *37*, 2419502 |
| 3 | 2 | 1 | 900 | *ACS Nano* **2025**, *19*, 13016−13028 |
| 4 | 1 | 1 | 630 | *Adv. Funct. Mater*. **2025**, e13773 |
| 5 | 1 | 1 | 3150 | *J. Am. Chem. Soc.* **2024**, *146*, 30998−31011 |
| 6 | 1 | 1 | 1750 | *Nat. Commun.* **2024**, *15*, 9702 |
| 7 | 2 | 1 | 3000 | *J. Am. Chem. Soc.* **2024**, *146*, 6199−6208 |
| 8 | 1 | 1 | 300 | *Nat. Commun.* **2024**, *15*, 302 |
| 9 | 1 | 1 | 1200 | *Adv. Funct. Mater*. **2024**, *34*, 2313358 |
| 10 | 1 | 0.5 | 2250 | *Chem. Sci.* **2024**, *15*, 1488–1497 |

**Table S4.** Comparative analysis of key performance metrics (energy density, electrolyte to active material ratio, rate capability, long-term cycling) and cost considerations between this work and state-of-the-art Zn–$I_2$ battery systems reported in recent years.

| | | Button cell | | | | | | | Cost | Pouch cell | | |
|---|---|---|---|---|---|---|---|---|---|---|---|---|
| | | | | Rate capability | | | | | | | | |
| No. | Reference | Current density (A $g^{-1}$) | Cycle life (cycle) | High current density (A $g^{-1}$) | High current density capacity (mAh $g^{-1}$) | Low current density (A $g^{-1}$) | Low current density capacity (mAh $g^{-1}$) | Capacity retention rate (High/ Low) | Electrolyte additives (US$ $kg^{-1}$) | Energy density (Wh/kg) | Cycle life (cycle) | Electrolyte-to-active-material ratio |
| 1 | This work | 20 | 50000 | 20 | 169 | 1 | 203 | 0.83 | 44 | 107 | 500 | 3.7 |
| 2 | *Energy Storage Mater.* **2025**, *81*, 104487. | 1 | 800 | 15 | 217 | 1 | 400 | 0.54 | | 34.3 | 150 | |
| 3 | *Adv. Mater.* **2025**, *37* (41), e05342. | 5 | 6000 | 5 | 388.9 | 1 | 754.1 | 0.52 | | 77.73 | 100 | |
| 4 | *Energy Environ. Sci.* **2025**, *18* (10), 4801–4810. | 5 | 330 | 10 | 128 | 0.2 | 219.5 | 0.58 | | | 100 | 3 |
| 5 | *Adv. Mater.* **2026**, e23132. | 0.1 | 175 | | | | | | | 34.3 | 1100 | |
| 6 | *Energy Storage Mater.* **2025**, *81*, 104525. | 2 | 12000 | 4 | 140 | 0.5 | 171 | 0.81 | | | 50 | 13 |
| 7 | *Chem. Eng. J.* **2025**, *526*, 171268. | 2 | 6000 | 6 | 340 | 0.5 | 760 | 0.44 | | 688 | 2000 | |
| 8 | *Adv. Mater.* **2026**, e18824. | | 3000 | | | | | | | | 1000 | 4.58 |
| 9 | *Energy Storage Mater.* **2026**, *84*, 104837., | 1 | 100 | 16 | 181.9 | 0.2 | 443.8 | 0.41 | | 185.8 | 50 | |
| 10 | *Energy Storage Mater.* **2026**, *84*, 104772. | 2 | 12000 | 20 | 103.3 | 1 | 201.5 | 0.51 | | 63.8 | 100 | |
| 11 | *Nat. Commun.* **2022**, *13*, 2283. | 8 | 12000 | | | | | | | 151 | 100 | |
| 12 | *Adv. Mater.* **2024**, *36*, 2314247. | 5 | 5000 | 15 | 516 | 1 | 730 | 0.70 | | 890 | 1000 | |
| 13 | *Advanced Energy Materials 2025, 15, 2404450* | 10 | 4000 | 10 | 154.5 | 0.1 | 286.9 | 0.53 | 168.55 | | | |
| 14 | *Nature Communications 2025, 16, 1800* | 1.2 | 1000 | | | | | | 30,000,000. | 250 | | |
| 15 | *Energy Storage Materials 2024, 70, 103449* | 2 C | 1000 | | | | | | 51.84 | | 200 | |
| 16 | *Nano-Micro Letters 2024, 16, 164* | 1 C | 300 | | | | | | 48.60 | | | |
| 17 | *Energy & Environmental Science 2024, 17, 8349–8359* | 1 | 1000 | | | | | | 167.31 | | 150 | 3.5 |
| 18 | *Angewandte Chemie International Edition 2024, 63, e202403695* | 0.5 | 300 | | | | | | 284.46 | | | |
| 19 | *Energy & Environmental Science 2025, 18, 1560–1571* | 1 | 1000 | | | | | | 140.45 | | 200 | 10.1 |
| 20 | *Energy Storage Materials 2025, 82, 104609* | 2 | 3000 | | | | | | 2472.81 | | | |
| 21 | *Angewandte Chemie International Edition 2023, 62, e202312193* | 0.5 | 1000 | 5 | 70.2 | 0.5 | 210.3 | 0.33 | 203,000.00 | | 200 | 2.6 |
| 22 | *Journal of the American Chemical Society 2024, 146, 10812–10821* | 1 | 3000 | | | | | | 196.11 | 380 | 3000 | 10 |
| 23 | *Journal of the American Chemical Society 2025, 147, 8523–8533* | 8 | 20000 | | | | | | 224.63 | | | |
| 24 | *Journal of the American Chemical Society 2025, 147, 27640–27650* | 0.2 | 500 | 5 | 130.1 | 0.1 | 157.6 | 0.82 | 560.20 | | | |
| 25 | *Advanced Materials 2025, 37, 11484* | 20 | 100000 | | | | | | 173.63 | | 50 | 2.56 |
| 26 | *J. Energy Storage* **2024**, *97*, 112760. | 5 | 45000 | 5 | 130.3 | 0.5 | 212.8 | 0.61 | | | | |
| 27 | *Energy Storage Mater.* **2025**, *74*, 103981. | 1 | 5000 | 1 | 120.17 | 0.2 | 205.44 | 0.58 | | | 500 | |
| 28 | *Adv. Energy Mater.* **2025**, e05649. | 0.2 | 1500 | 4 | 175.5 | 0.5 | 303.5 | 0.57 | | | | |
| 29 | *Angew. Chem. Int. Ed.* **2024**, *63* (25), e202403187. | 10 | 10000 | 10 | 240 | 1 | 250 | 0.96 | | | | |
| 30 | *Energy Environ. Sci.* **2021**, *14* (1), 407–413. | 3 | 2750 | 5 | 126.27 | 0.5 | 207 | 0.61 | | | | |
| 31 | *Adv. Energy Mater.* **2024**, | 0.2 | 1000 | 5 | 83.3 | 0.2 | 213.4 | 0.39 | | | 100 | |

| | | | | | | | | | | |
|---|---|---|---|---|---|---|---|---|---|---|
| | *14* (17), 2304110. | | | | | | | | | |
| 32 | *Nano Energy* **2025**, *138*, 110884. | 1 | 500 | 15 | 195 | 1 | 372 | 0.52 | | |
| 33 | *Chem. Eng. J.* **2025**, *525*, 170719. | 2 | 12000 | 5 | 159.7 | 0.2 | 195.8 | 0.81 | | 500 |
| 34 | *ACS Nano* **2025**, *19* (2), 2901–2908. | 1 | 350 | 3 | 272 | 0.5 | 422 | 0.64 | | |
| 35 | *Adv. Mater.* **2024**, *36* (32), 2405473. | 0.4 | 1500 | 4 | 438 | 0.2 | 614 | 0.71 | | 100 |
| 36 | *Nano-Micro Lett.* **2023**, *15* (1), 126. | 5 | 50000 | 15 | 73.89 | 0.3 | 139.6 | 0.52 | | 125 |
| 37 | *Nano Lett.* **2025**, *25* (16), 6661–6669. | 0.2 | 500 | 4 | 182 | 0.2 | 216 | 0.84 | | |
| 38 | *Angew. Chem. Int. Ed.* **2024**, *63* (39), e202404784. | 2 | 5000 | 40 | 200 | 2 | 450 | 0.44 | | |
| 39 | *Chem. Eng. J.* **2025**, *524*, 169846. | 0.5 | 600 | 1 | 125 | 0.1 | 200 | 0.62 | | 275 |
| 40 | *Energy Storage Mater*. **2025**, *76*, 104113. | 5 | 60000 | 10 | 125.1959 | 0.2 | 187.7 | 0.66 | | |
| 41 | *Nano Energy* **2022**, *98*, 107278. | 4.5 | 10000 | 4.5 | 129 | 0.5 | 235 | 0.54 | | |
| 42 | *J. Energy Storage* **2025**, *137*, 118643. | 10 | 7000 | 15 | 125 | 0.1 | 263.9 | 0.47 | | |
| 43 | *ACS Nano* **2025**, *19* (27), 25438–25454. | 0.2 | 500 | 5 | 189.7 | 0.5 | 241.7 | 0.78 | | 1600 |
| 44 | *ACS Nano* **2025**, *19* (36), 32533–32545. | 2 | 8000 | 10 | 173 | 1 | 240 | 0.72 | | 100 |
| 45 | *Energy Storage Mater.* **2025**, *78*, 104246. | 1 | 8000 | 5 | 130.1 | 0.1 | 169.4 | 0.76 | | |
| 46 | *Adv. Funct. Mater.* **2026**, *36* (4), e13773. | 2 | 16000 | 5 | 92.9 | 0.2 | 224.5 | 0.41 | | 300 |
| 47 | *Adv. Mater.* **2024**, *36* (38), 2408317. | 2 | 10000 | 2 | 166.9 | 0.05 | 279.9 | 0.59 | | 60 |
| 48 | *Adv. Funct. Mater.* **2025**, *35* (6), 2415107. | 4 | 40000 | 10 | 120.85 | 1 | 202.84 | 0.59 | | 1000 |
| 49 | *Nano Energy* **2025**, *144*, 111390. | 20 | 8000 | 10 | 108 | 0.5 | 165 | 0.65 | | 200 |
| 50 | *Adv. Energy Mater.* **2023**, *13* (24), 2300922. | 1 | 5700 | 3 | 180 | 0.5 | 206 | 0.87 | | |
| 51 | *Adv. Funct. Mater.* **2025**, *35* (47), 2509582. | 5 | 20000 | 10 | 202 | 0.2 | 386 | 0.52 | | |
| 52 | *Nat. Commun.* **2023**, *14* (1), 1856. | 2 | 2000 | 5 | 75 | 0.5 | 210 | 0.35 | | 300 |
| 53 | *Angew. Chem. Int. Ed.* **2024**, *63* (49), e202410848. | 16 | 320000 | 16 | 118 | 1 | 224 | 0.524 | | |
| 54 | *Energy Environ. Sci.* **2024**, *17* (18), 6666–6675. | 2 | 1800 | 10 | 241 | 0.5 | 391 | 0.61 | | |
| 55 | *Adv. Mater.* **2026**, *38* (6), e13389. | 0.5 | 500 | 8 | 300 | 0.5 | 604 | 0.49 | | |
| 56 | *Adv. Energy Mater.* **2025**, e05589. | 20 | 50000 | 20 | 122.2 | 1 | 327.3 | 0.37 | | 100 |
| 57 | *Small* **2025**, *21* (51), e10396. | 1 | 5000 | 5 | 113 | 0.1 | 183 | 0.61 | | |
| 58 | *Adv. Funct. Mater.* **2025**, e13527. | 1 | 10000 | 3 | 158.3 | 0.1 | 231.1 | 0.68 | | |
| 59 | *Adv. Funct. Mater.* **2025**, *35* (26), 2422677. | 8 | 40000 | 8 | 131 | 0.5 | 178 | 0.73 | | |
| 60 | *Small* **2026**, e00044. | 10 | 25000 | 8 | 154.08 | 0.5 | 198.76 | 0.77 | | |
| 61 | *Energy Storage Mater.* **2023**, *63*, 103019. | 2 | 1000 | 20 | 120 | 0.5 | 202 | 0.59 | | |
| 62 | *ACS Mater. Lett.* **2022**, *4* (10), 1872–1881. | 10 | 40000 | 5 | 90 | 0.2 | 116 | 0.77 | | 1000 |
| 63 | *Energy Environ. Sci.* **2025**, *18* (12), 5998–6008. | 2 | 16000 | 15 | 120.2 | 0.5 | 190.6 | 0.63 | | 210 |
| 64 | *Adv. Funct. Mater.* **2026**, *36* (8), e16000. | 5 | 10000 | 10 | 113 | 1 | 183 | 0.61 | | |
| 65 | *Nano-Micro Lett.* **2022**, *14* (1), 208–221. | 1 | 1000 | 5 | 103.1 | 0.2 | 145.6 | 0.70 | | |
| 66 | *Chem. Eng. J.* **2025**, *524*, 169752. | 10 | 12000 | 2 | 110 | 0.1 | 170 | 0.64 | | |
| 67 | *Energy Storage Mater.* **2025**, *75*, 103994. | 2 | 9000 | 8 | 84.6 | 0.3 | 197.3 | 0.42 | | |
| 68 | *Nano Lett.* **2022**, *22* (6), 2538–2546. | 1 | 1000 | 4 | 47.8 | 0.2 | 123.4 | 0.38 | | |
| 69 | *Adv. Mater.* **2024**, *36* (16), 2311914. | 25 | 220000 | 50 | 75.2 | 5 | 210.9 | 0.35 | | |
| 70 | *J. Energy Storage* **2025**, | 10 | 4000 | 2 | 123.42 | 0.1 | 143.86 | 0.85 | | |

| | | | | | | | | | | |
|---|---|---|---|---|---|---|---|---|---|---|
| | *120*, 116495. | | | | | | | | | |
| 71 | *ACS Nano* **2023**, *17* (20), 20643–20653. | 5 | 20000 | 2 | 162 | 0.2 | 241 | 0.67 | | |
| 72 | *Chem. Eng. J.* **2025**, *521*, 166472. | 4 | 55000 | 4 | 137 | 0.2 | 202 | 0.68 | | |
| 73 | *Energy Environ. Mater.* **2026**, e70236. | 2 | 13000 | 2 | 154.3 | 0.1 | 249.7 | 0.61 | | |
| 74 | *ACS Energy Lett.* **2026**, *11* (1), 681–690. | 5 | 12000 | 10 | 161 | 0.5 | 249 | 0.64 | | |
| 75 | *Angew. Chem. Int. Ed.* **2024**, *63* (51), e202411884. | 4 | 30000 | 6 | 169.8 | 1 | 202.1 | 0.84 | | 750 |
| 76 | *Nano Energy* **2025**, *138*, 110876. | 1 | 10000 | 3 | 117.5 | 0.1 | 155.5 | 0.75 | | |
| 77 | *Small* **2025**, *21* (13), 2500223. | 0.5 | 2600 | 5 | 102.9 | 0.1 | 209.9 | 0.49 | | |
| 78 | *J. Energy Storage* **2024**, *88*, 111538. | 2 | 3800 | 2 | 123 | 0.1 | 201 | 0.61 | | |
| 79 | *Adv. Funct. Mater.* **2025**, *35* (39), 2505132. | 1 | 1000 | 8 | 74 | 0.5 | 153 | 0.48 | | |
| 80 | *Adv. Energy Mater.* **2024**, *14* (44), 2402846. | 2 | 5000 | 2 | 122.8 | 0.05 | 190.7 | 0.64 | | 100 |
| 81 | *Angew. Chem. Int. Ed.* **2025**, *64* (42), e202514375. | 2 | 1000 | 40 | 273.55 | 1 | 484.36 | 0.56 | | 500 |
| 82 | *Energy Environ. Sci.* **2024**, *17* (1), 323–331. | 4 | 15000 | 20 | 86.8 | 4 | 120.3 | 0.72 | | |
| 83 | *Chem. Eng. J.* **2025**, *514*, 162992. | 0.5 | 1000 | 3 | 118.989 | 0.2 | 146.9 | 0.81 | | |
| 84 | *Energy Environ. Mater.* **2025**, *8* (5), e70045. | 1 | 1200 | 5 | 89.4 | 0.2 | 191.3 | 0.46 | | |
| 85 | *Nat. Commun.* **2025**, *16* (1), 5565. | 10 | 50000 | 20 | 135.5 | 0.3 | 205.4 | 0.65 | | 1400 |
| 86 | *Adv. Mater.* **2020**, *32* (38), 2004240. | 1,92 | 6000 | 1.28 | 102.6 | 0.16 | 203 | 0.50 | | |

## 4. References


[55] G. Kresse, J. Hafner, *Phys. Rev. B* **1993**, *47*, 558–561.

[56] G. Kresse, J. Hafner, *Phys. Rev. B* **1994**, *49*, 14251–14269.

[57] J. P. Perdew, K. Burke, *Phys. Rev. Lett.* **1996**, *77*, 3865–3868.

[58] G. Kresse, D. Joubert, *Phys. Rev. B* **1999**, *59*, 1758–1775.

[59] S. Grimme, J. Antony, S. Ehrlich, H. Krieg, *J. Chem. Phys.* **2010**, *132*, 154104.

[60] K. Momma, F. Izumi, *J. Appl. Crystallogr.* **2011**, *44*, 1272–1276.

[61] L. Martínez, R. Andrade, E. G. Birgin, J. M. Martínez, *J. Comput. Chem.* **2009**, *30*, 2157–2164.

[62] M. J. Robertson, Y. Qian, M. C. Robinson, J. Tirado-Rives, W. L. Jorgensen, *J. Chem. Theory Comput.* **2019**, *15*, 2734–2742.

[63] B. Doherty, X. Zhong, S. Gathiaka, B. Li, O. Acevedo, *J. Chem. Theory Comput.* **2017**, *13*, 6131–6145.

[64] M. J. Abraham, T. Murtola, R. Schulz, S. Páll, J. C. Smith, B. Hess, E. Lindahl, *SoftwareX* **2015**, *1-2*, 19–25.

[65] W. Humphrey, A. Dalke, K. Schulten, **1996**, *14*, 33–38.

[66] G. A. Kaminski, R. A. Friesner, J. Tirado-Rives, W. L. Jorgensen, *J. Phys. Chem. B* **2001**, *105*, 6474–6487.

[67] A. Stukowski, K. Albe, *Modell. Simul. Mater. Sci. Eng.* **2010**, *18*, 085001.

[68] C. Adamo, V. Barone, *J. Chem. Phys.* **1999**, *110*, 6158–6170.

[69] F. Weigend, R. Ahlrichs, *Phys. Chem. Chem. Phys.* **2005**, *7*, 3297-3305.

[70] P. C. C. Physics, *Phys. Chem. Chem. Phys.* **2006**, *8*, 1057–1065.

[71] M. Frisch, G. Trucks, H. Schlegel, G. Scuseria, M. Robb, J. Cheeseman, G. Scalmani, V. Barone, B.Mennucci, G. Petersson, H. Nakatsuji, M. Caricato, X. Li, H. Hratchian, A. Izmaylov, J. Bloino, G. Zheng, J. Sonnenberg, M. Hada, M. Ehara, K. Toyota, R. Fukuda, J. Hasegawa, M. Ishida, T. Nakajima,

Y. Honda, O. Kitao, H. Nakai, T. Vreven, J. Montgomery Jr, J. Peralta, F. Ogliaro, M. Bearpark, J. Heyd,

E. Brothers, K. Kudin, V. Staroverov, R. Kobayashi, J. Normand, K. Raghavachari, A. Rendell, J. Burant,

S. Iyengar, J. Tomasi, M. Cossi, N. Rega, N. Millam, M. Klene, J. Knox, J. Cross, V. Bakken, C. Adamo,

J. Jaramillo, R. Gomperts, R. Stratmann, O. Yazyev, A. Austin, R. Cammi, C. Pomelli, J. Ochterski, R. Martin, K. Morokuma, V. Zakrzewski, G. Voth, P. Salvador, J. Dannenberg, S. Dapprich, A. Daniels, Ö.

Farkas, J. Foresman, J. Ortiz, J. Cioslowski, D. Fox, *Gaussian 16, Revision C.02.* **2016**, Gaussian, Inc., Wallingford, CT, USA.

[72] S. Grimme, S. Ehrlich, L. Goerigk, *J. Comput. Chem.* **2011**, *32*, 1456–1465.

[73] T. Lu, F. Chen, *J. Comput. Chem.* **2011**, *33*, 580–592.